

Fronts and nonlinear waves in a simplified shallow-water model of the atmosphere with moisture and convection

François Bouchut,¹ Julien Lambaerts,² Guillaume Lapeyre,² and Vladimir Zeitlin^{2,a)}

¹*Département de Mathématiques et Applications, ENS/CNRS, 45 Rue d'Ulm, 75005 Paris, France*

²*Laboratoire de Météorologie Dynamique/IPSL, UPMC-ENS/CNRS, 24 Rue Lhomond, 75005 Paris, France*

(Received 10 June 2009; accepted 29 October 2009; published online 30 November 2009)

We describe a shallow-water type atmospheric model which includes the transport of moisture as well as related precipitation and convection effects. The model combines hydrodynamic nonlinearity of the standard shallow-water model with the intrinsic nonlinearity due to the precipitation threshold. It allows for both theoretical treatment by the method of characteristics and efficient numerical resolution using shock-capturing finite-volume schemes. Linearized in the dynamical sector, the model adequately reproduces the propagation of the edge of precipitation regions (precipitation fronts) found in earlier studies. Results of numerical experiments on simple wave scattering upon a moisture front are in agreement with analytical results and highlight the role of dissipative reflector played by precipitating zones. We also analyze the evolution of a disturbance propagating in a uniformly saturated region and obtain criteria for precipitation front formation. Finally, we simulate wave breaking as an example of essentially nonlinear phenomenon and show how moist effects modify the classical shock formation scenario. © 2009 American Institute of Physics. [doi:10.1063/1.3265970]

I. INTRODUCTION

Water vapor plays a fundamental role in the climate system as a greenhouse gas but also through the latent heat release during condensation.¹ This last effect is important for the large-scale atmospheric dynamics, especially in tropical areas. Because the deep convection zones are still too small to be resolved explicitly in general circulation models, at present moist convection is parametrized in terms of large-scale variables. Various parametrizations are used in numerical models (i.e., Arakawa and Schubert²), the Betts–Miller scheme being the most common.³ Based on convective quasiequilibrium, it expresses latent heat release and precipitation in terms of linear relaxation of the specific humidity toward an equilibrium profile, once moisture exceeds the saturation value. Such threshold effect (which, among others, creates a boundary between nonprecipitating and precipitating regions) is essentially nonlinear and drastically changes the way the system should be analyzed, whatever the smallness of perturbations of the dynamical variables. For example, the traditional harmonic wave wisdom is not applicable anymore in precipitating regions. A favorable moisture environment can also increase dramatically the growth of synoptic perturbations through this nonlinearity.^{4,5} Other specific phenomena, such as precipitation fronts,^{6,7} emerge. Although the existing literature on the interaction of moist convection and large-scale circulation is vast (e.g., Refs. 8–11), the fundamental dynamical aspects of precipitating systems are not often addressed (see, however, Refs. 4 and 12–16 for investigation of the role of moist processes in dynamics).

Gill,¹⁷ in his pioneering work, studied the fundamental dynamical issues related to precipitation using a heuristic

linear shallow-water (SW in what follows) equations for velocity and (potential) temperature in one spatial dimension, combined with a linearized transport equation for water vapor. An immediate relaxation of humidity was used in order to couple potential temperature and water vapor equations, and the behavior of disturbances developing from an initial temperature perturbation in a saturated atmosphere was analyzed. The method of characteristics allowed to describe the edge between dry and moist regions. However (see below) the success of such analysis strongly relies on the specific initial conditions.

Recently Majda and co-workers^{6,7} developed a theory of precipitation fronts by using basically the same model (linear, except for precipitation and latent heat release effects) as that of Gill.¹⁷ This model was motivated by vertical mode decomposition and truncation at the lowest order. Majda and co-workers were interested in precipitation fronts, treated as discontinuities in the spatial derivatives of the dynamical variables at the boundary between dry and moist regions, and again worked in the limit of relaxation time tending to zero. By analyzing the Rankine–Hugoniot (RH) conditions for the gradients, three possible types of precipitation fronts were identified. These results were extended to finite relaxation times in Ref. 18. The effect of precipitation on the propagation of equatorial waves in the precipitation front framework was also discussed in Ref. 19.

The goal of the present paper is to derive a SW-type model that would combine the nonlinearity due to precipitation with genuine hydrodynamic nonlinearity of the primitive equations, and to analyze their combined effects in the fundamental dynamical processes. Our motivation is to have a simple yet self-consistent and reliable tool for both theoretical and numerical analysis of moist dynamics. In fact, the two are interconnected, as shock-capturing high-resolution

^{a)}Electronic mail: zeitlin@lmd.ens.fr.

finite-volume numerical schemes²⁰ exist for rotating shallow-water (RSW) models, and were exhaustively tested in geophysical fluid dynamics applications (e.g., Ref. 21). Inclusion of a tracer (moisture) in these models is trivial, and incorporation of a relaxation scheme for precipitation is straightforward. Thus, a fully nonlinear “moist SW” model generalizing earlier linear moist SW equations would allow for a direct high-resolution front-capturing numerical simulations of fundamental dynamical processes in precipitating systems. Other studies (e.g., Refs. 22 and 23) using SW-type models examined the dynamical role of latent heat release. However, in these models, convection was just parametrized using wind convergence and no moisture equation was used.

The paper is organized as follows. In Sec. II, we propose a heuristic derivation of the model and then analyze its basic properties using the standard tools for hyperbolic systems (characteristics, Riemann invariants). Numerical experiments are performed in Sec. III to check if the model reproduces earlier results reported in literature^{6,7,17} on the front propagation and to benchmark the numerical scheme. As typical examples/benchmarks, we have chosen the interaction between a simple wave and a stationary humidity front (Sec. III B) and the evolution of a small perturbation in a uniformly saturated region (Sec. III C). The nonlinear stage of evolution of a simple wave in the presence of moisture is considered as a typical example of combined hydrodynamic and precipitation nonlinearities in Sec. III D. Section IV contains summary and discussion. A more detailed discussion of the model and its generalizations in view of the moist enthalpy (ME) conservation principle are presented in Appendix A. A generalization of the moisture relaxation scheme is described in Appendix B and a sketch of its numerical implementation is given in Appendix C.

II. THE MODEL: “MOIST-CONVECTIVE” ROTATING SHALLOW WATER

A. Introducing moist convection in shallow-water models

Let us remind (cf., e.g., Ref. 24) that RSW models (one- or multilayer) can be obtained by vertical averaging of primitive equations between pairs of material surfaces, and by applying the mean-field hypothesis, i.e., replacing the horizontal velocities by their averaged values (corrections can be incorporated via the turbulence viscosity/diffusivity closures, if necessary). Traditionally, the average density (potential temperature in the atmospheric case) is not allowed to vary, otherwise the generalized SW equations (so-called Ripa’s equations^{25,26}) arise instead of the standard ones. We shall adopt below the standard hypothesis (the case of Ripa’s equations is briefly discussed in Appendix A). This physically means that the energy release due to precipitation does not increase the average potential temperature, but rather produces convection and a corresponding mass flux (see a more detailed discussion in Appendix A).

As a starting point we take dry hydrostatic primitive equations with pseudoheight

$$z = z_0 \left[1 - \left(\frac{p}{p_s} \right)^\kappa \right], \quad z_0 = \frac{p_s}{\kappa g \rho_s}, \quad \kappa = \frac{R}{c_p}, \quad p_s = \text{const} \quad (2.1)$$

as the vertical coordinate,²⁷ and average them between two material surfaces (z_1, z_2) such that $dz_{1,2}/dt = w|_{1,2}$, where w is vertical velocity in pseudoheight coordinates. We take the bottom surface, $z_1(x, y, t)$, corresponding to constant geopotential (physical ground), and the top one to be isobaric, $z_2 = \text{const}$. We obtain in this way the usual RSW equations for air columns,

$$\partial_t \mathbf{v} + (\mathbf{v} \cdot \nabla) \mathbf{v} = -g \nabla h - f \hat{\mathbf{z}} \times \mathbf{v}, \quad (2.2)$$

$$\partial_t h + \nabla \cdot (\mathbf{v} h) = 0, \quad (2.3)$$

where $\mathbf{v} = (u, v)$ is the vertically averaged horizontal velocity, ∇ is the horizontal gradient, $\hat{\mathbf{z}}$ is the unit vector in the z -direction, g is the gravity acceleration, and $h = z_2 - z_1$ is the thickness of the layer in pseudoheight coordinates.

We want now to include moisture with precipitation sink and the related convective motions in the model (for simplicity, we will not include the evaporation sources in what follows). Of course, the neatest way to do this would be to vertically average the moist primitive equations, along the lines of the derivation of the “dry” RSW equations sketched above. However, due to the intrinsic nonlinearity of the equation of state of the moist air, cf. Ref. 9, this task turns to be extremely complicated and necessitates a number of *ad hoc* hypotheses to proceed. We choose therefore another approach in the spirit of turbulence closures. We will suppose that the total amount of water vapor in the air column $Q = \int_{z_1}^{z_2} q dz$, i.e., the specific humidity q integrated over the layer, is conserved modulo the precipitation sink P . Obviously, the related latent heat release does not directly influence the horizontal momentum Eq. (2.2) and the closure should consist in coupling the moisture equation and thickness equations.

We thus change the kinematic boundary condition at the upper surface to allow for mass exchanges,

$$w_2 = \frac{dz_2}{dt} + W \quad (2.4)$$

and suppose that the convective vertical velocity W is directly proportional to P : $W = \beta P$ (c.f. Fig. 1). In this way we obtain the following equations:

$$\partial_t \mathbf{v} + (\mathbf{v} \cdot \nabla) \mathbf{v} = -g \nabla h - f \hat{\mathbf{z}} \times \mathbf{v}, \quad (2.5)$$

$$\partial_t h + \nabla \cdot (\mathbf{v} h) = -\beta P, \quad (2.6)$$

$$\partial_t Q + \nabla \cdot (\mathbf{v} Q) = -P. \quad (2.7)$$

It should be noted that a similar representation is used to model convection in the SW models of the deep ocean (e.g., Ref. 28). In consequence, the model will be referred below as moist-convective RSW (MC-RSW).

The second element of the closure is parametrization of the precipitation in terms of the dynamical variables of the

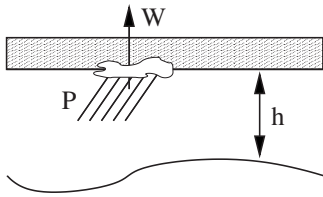


FIG. 1. Sketch of the representation of the moisture effects in the MC-RSW model. Deep convection regions are associated with an additional vertical velocity supposed to be proportional to the precipitation: $W = \beta P$.

model. We will use below a simple relaxation closure expressing P in terms of Q and its saturation value Q_s ,

$$P = \frac{Q - Q_s}{\tau} H(Q - Q_s), \quad (2.8)$$

where τ is the relaxation time and $H(\cdot)$ is the Heaviside function. Such relaxation is close in spirit to the Betts–Miller scheme widely used in general circulation models (GCMs), although the genuine one corresponds to adjustment of the specific humidity q to a vertical convective reference profile $q^c(z)$.³ The closure falls in the class of “quasiequilibrium closures” which relax the excess instability (here simply the excess moisture) to its critical value. The immediate relaxation limit $\tau \rightarrow 0$ is usually referred to as “strict quasiequilibrium,” see Ref. 8. For simplicity, the saturation value Q_s is chosen as constant but it can also depend on the layer thickness h as discussed in Appendix B.

An important observation is that by combining Eqs. (2.6) and (2.7) we find a local conservation law for the combination

$$m = h - \beta Q, \quad (2.9)$$

which corresponds to the moist enthalpy (ME). This implies that for saturated atmosphere $Q = Q_s$ with a small perturbation $\{\mathbf{v}, \eta\}$ over a state of rest $\{0, H_0\}$, such that

$$\partial_t \eta + (H_0 - \beta Q_s) \nabla \cdot \mathbf{v} = 0, \quad (2.10)$$

the static stability is smaller than the dry static stability if the coefficient β is positively definite: $H_0 - \beta Q_s < H_0$, in agreement with the standard notion of reduced stability in precipitating regions.¹³ An alternative derivation of the MC-RSW model may be obtained by imposing the ME conservation as a closure hypothesis. It is presented in the Appendix A.

Thus, the hydrodynamic nonlinearity of the RSW is preserved in the model, while linearization in one dimension without rotation ($v=0, f=0$) gives the equations used in earlier studies^{6,7,17,18} upon the change in variables $h \rightarrow -\theta$. Note that this change in variables allows us to make connection of our model to the pioneering papers on tropical dynamics by Gill,^{29,30} where convection effects were parametrized as a mass source in the linear SW equations. This line of argument was pursued under the so-called weak temperature gradient approximation in Refs. 31 and 32. A mass source in Gill’s SW equations for θ becomes a mass sink in the equations for h , as in Eq. (2.6)—see also discussion in Appendix A.

B. Mass and energy balances

Since moisture effects result in the source terms in the MC-RSW equations, it is important to understand their role in the mass and energy balances. We should emphasize that no viscosity nor diffusion were introduced in the hydrodynamical sector of the model.

The mass of the fluid layer in pseudoheight coordinates is obtained by vertical integration of the pseudodensity $r = \rho_s p_s^{\kappa-1} p^{1-\kappa}$. This quantity weakly varies in the vertical and is considered approximately constant, see Ref. 27. In consequence, the mass of the layer is proportional to the layer thickness h : $\int r dz \approx rh$. It appears then that moist processes reduce the total mass of the layer in the MC-RSW model. Nevertheless, the conservation of the ME $m = h - \beta Q$ imposes a constraint on the mass variations because

$$\iint dx dy h(t) > \iint dx dy \beta Q(t) > 0 \quad (2.11)$$

if $h(t_0) - \beta Q(t_0) > 0$. Allowing a (limited) mass loss in the model means that it should be interpreted as the lower atmospheric layer part of a more complete multilayer model. Yet, such mass loss will obviously affect the energy balance.

In their one-dimensional (1D) nonrotating linearized model ($v=f=0$), Frierson *et al.*⁶ showed that precipitation can either increase or dissipate the dry energy depending on the sign of the perturbation. A similar result was obtained in Ref. 17 for the moist linearized RSW and in Ref. 4 for a two-layer moist baroclinic model. In all of these papers, the energy principle had to be modified to include moisture and to identify properly the dissipation mechanisms.

The dry energy density e in MC-RSW is expressed in the same way as in the standard RSW,

$$e = \frac{1}{2}(\mathbf{v}^2 h + gh^2). \quad (2.12)$$

The evolution of the associated total energy $E = \iint e dx dy$ follows:

$$\begin{aligned} \partial_t E = & - \iint dx dy \nabla \cdot \left[\left(\frac{\mathbf{v}^2}{2} + gh \right) \mathbf{v} h \right] \\ & - \beta \iint dx dy \left(\frac{\mathbf{v}^2}{2} + gh \right) P. \end{aligned} \quad (2.13)$$

The first term in the right hand side is standard and vanishes for isolated systems, and the second is negatively definite for nonzero P and $\beta > 0$. We thus observe that precipitation always dissipates the total dry energy of the system. This dissipation is related to the mass loss in the absence of any compensating process (e.g., radiative cooling). Note that the difference in this result with respect to other studies^{4,6,17} is due to the obvious fact that the full layer thickness h is positively definite unlike its perturbation. It should be stressed that it is the ME that is the relevant quantity for the moist processes, and its conservation in the model is built in. Note also that for multilayer models with different mean potential temperatures of the layers, the energy budget will be different.

C. Hyperbolicity and characteristic equations

Let us be reminded that a standard way of studying wave systems is the method of characteristics (e.g., Ref. 33). Solutions of the hyperbolic (\equiv wave) system can be expressed via Riemann variables propagating along the characteristic curves in (x, t) -space. All characteristic velocities are real if the system is hyperbolic. For a quasilinear system in one spatial dimension with N variables $u_i(x, t)$,

$$\partial_t u_i + A_{ij}(x, t, \mathbf{u}) \partial_x u_j + B_i = 0, \quad (2.14)$$

the characteristic velocities $c_i = dx/dt$ are the eigenvalues of the matrix A_{ij} corresponding to the left eigenvectors $V_i = \{V_{i1}, \dots, V_{iN}\}$. The system, thus, can be rewritten in the form

$$V_{ij}(\partial_t + c_i \partial_x) u_j + V_{ij} B_j = 0 \quad (2.15)$$

or, equivalently, as

$$(\partial_t + c_i \partial_x) r_i + f_i(x, t, \mathbf{u}) = 0, \quad (2.16)$$

where r_i are the Riemann variables, which become invariants in the absence of B_i .

The method of characteristics is particularly appropriate for MC-RSW because the nonlinearity due to the threshold character of precipitation (formally expressed by the Heaviside function) prevents from using the standard Fourier (harmonic wave) decomposition. This is true even if the hydrodynamic part of the system is linearized (i.e., for small-amplitude perturbations over the state of rest). Indeed, a harmonic wave in regions of negative divergence of the velocity field creates an excess of moisture and triggers precipitation leading to a nonlinear response.

The method of characteristics was used by Gill¹⁷ for a 1D linearized SW model in two different regions. Assuming that the relaxation is immediate ($\tau \rightarrow 0$), it was shown that the dry regions ($P=0$) and the “wet” regions ($P>0$) have their proper characteristic velocities. Such analysis allows to describe the evolution of the boundary point between the two regions. However, Gill’s solution of the initial-value problem explicitly relies on specific initial conditions and is not universal, as we will show in Sec. III.

We adopt a more general approach and derive the characteristic equations of the 1D MC-RSW model (by suppressing the y -dependence of all dynamical variables the model, in fact, becomes “1.5 dimensional” (1.5D) as it still contains v , the velocity in the “passive” direction). We analyze the model both for finite relaxation time (τ), and in the limit of immediate relaxation $\tau \rightarrow 0$ with special emphasis on hyperbolicity, which is the *sine qua non* condition of applicability of the method. The characteristic equations will allow us to clearly identify the role of moist effects in fully nonlinear dynamics.

1. Finite relaxation time

If the relaxation time is finite ($\tau \neq 0$), systems (2.5)–(2.7) in 1.5D is first order quasilinear and hyperbolic, and can be readily rewritten in the characteristics form

$$(\partial_t + c_v \partial_x) r_v = -fu, \quad (2.17)$$

$$(\partial_t + c_q \partial_x) r_q = -\left(1 - \frac{\beta Q}{h}\right) \frac{P}{h}, \quad (2.18)$$

$$(\partial_t + c_{\pm} \partial_x) r_{\pm} = f v \mp \beta \sqrt{\frac{g}{h}} P, \quad (2.19)$$

where the Riemann variables, $\{r_v, r_q, r_+, r_-\}$, are defined as

$$r_v = v, \quad r_q = \frac{Q}{h}, \quad \text{and} \quad r_{\pm} = u \pm 2\sqrt{gh}. \quad (2.20)$$

They evolve along their proper characteristic curves $dx/dt = c$ in the (x, t) -plane,

$$c_v = c_q = u \quad \text{and} \quad c_{\pm} = u \pm \sqrt{gh}. \quad (2.21)$$

Equations (2.17) and (2.18) are conservation laws because their relative characteristic velocities are zero. Equation (2.19) defines propagating solutions and their relative characteristic velocity corresponds to the nonlinear gravity wave velocity of the standard SW model which is called the *dry velocity* ($c_d = \sqrt{gh}$) below. Without rotation ($f=0$), we observe that all Riemann variables are *invariant* in the nonprecipitating regions ($P=0$). However, in the precipitating region ($P>0$), the moist Riemann variable ($r_q \propto Q$) and the eastward propagating (r_+) variables are decreasing and the westward-propagating variable r_- is increasing. This fact allows us to anticipate a role of reflector played by precipitation in the propagation of simple waves, which will be confirmed below by direct numerical simulations (DNS). Note that there is no real asymmetry between eastward and westward solutions because Riemann variables are defined up to a constant, e.g., -1 , and may be exchanged $r_- \rightarrow -\tilde{r}_-$.

The mass nonconservation in the model due to convection imposes obvious restrictions on initial conditions. Because ME is conserved and serves as static stability parameter, initial ME should be positive: $m(t_0) = h(t_0) - \beta Q(t_0) > 0$. We also require Q to be positive such that $0 < \beta r_q < 1$.

2. Immediate relaxation

The relaxation time scale in the atmosphere is rather small (between 2 and 12 h) and, for large-scale motions, it is reasonable to assume that the relaxation is immediate: $\tau \rightarrow 0$. However, it is easy to make a straightforward but long-reaching observation: The limit $\tau \rightarrow 0$ corresponding to the strict quasiequilibrium hypothesis is singular and system (2.5)–(2.7) is not hyperbolic anymore. It becomes *piecewise hyperbolic* and matching rules should be prescribed at the boundaries between different hyperbolic regions. In the nonprecipitating zones ($P=0$), the same characteristic equations (2.17)–(2.19) as above are valid. Yet, in the precipitating zones ($P>0$) the system should be reanalyzed.

If we assume that in the precipitating region the moisture field has a typical time scale much shorter than the velocity field $|\partial_t q|/|q| = \tau^{-1} \gg |\partial_t(\nabla \cdot \mathbf{v})|/|\nabla \cdot \mathbf{v}|$, then the equation for the small perturbation of moisture about the saturated state $q = Q - Q_s > 0$ can be integrated in time assuming that the gradients are weak: $|\nabla \cdot (\mathbf{v}q)| \approx 0$,

$$\partial_t q \approx -\frac{q}{\tau} - Q_s \nabla \cdot \mathbf{v} \quad (2.22)$$

and

$$q_{\tau \rightarrow 0} \approx q_0 \exp\left[-\frac{t}{\tau}\right] + \tau Q_s \nabla \cdot \mathbf{v} \approx \tau Q_s \nabla \cdot \mathbf{v}. \quad (2.23)$$

By injecting this expression into P [Eq. (2.8)], we obtain a standard parametrization (e.g., Ref. 17),

$$P = -Q_s \nabla \cdot \mathbf{v}, \quad (2.24)$$

which directly links precipitation with wind convergence. We thus get a typical conditional CISK (Conditional Instability of the Second Kind)-parametrization since the pseudoheating source (βP) is proportional to the total convergence of moisture (cf. Ref. 12).

In this case, the MC-RSW system in the precipitating region ($P > 0$) becomes

$$\partial_t \mathbf{v} + (\mathbf{v} \cdot \nabla) \mathbf{v} = -g \nabla h - f \mathbf{k} \times \mathbf{v}, \quad (2.25)$$

$$\partial_t h + (\mathbf{v} \cdot \nabla) h = -(h - \beta Q_s) \nabla \cdot \mathbf{v}. \quad (2.26)$$

This is a quasilinear hyperbolic first order system and can be studied by the method of characteristics.

In 1.5D, the characteristic equations are

$$(\partial_t + c_v^m \partial_x) r_v^m = -f u, \quad (2.27)$$

$$(\partial_t + c_{\pm}^m \partial_x) r_{\pm}^m = f v, \quad (2.28)$$

where the moist Riemann variables are given by

$$r_v^m = v \quad \text{and} \quad r_{\pm}^m = u \pm 2\sqrt{g(h - \beta Q_s)}, \quad (2.29)$$

and propagate along their respective characteristic curves $dx/dt = c^m$,

$$c_v^m = u \quad \text{and} \quad c_{\pm}^m = u \pm \sqrt{g(h - \beta Q_s)}. \quad (2.30)$$

Equation (2.27) is identical to Eq. (2.17) and Eq. (2.28) is the moist equivalents of Eq. (2.19). We notice here that the moist Riemann variables are *always invariant* in the nonrotating case ($f=0$). The relative characteristic velocity of the propagating solutions will be called the *moist velocity* following Frierson *et al.*⁶ and is weaker than the dry velocity ($\beta > 0$),

$$c_m = \sqrt{g(h - \beta Q_s)} < c_d = \sqrt{gh}. \quad (2.31)$$

It can be interpreted as a velocity of moisture-coupled waves. The fact that it is always lower than the dry gravity wave velocity is usually explained in literature¹³ by the reduction in the static stability of the atmosphere due to the moist convection.

Thus, in the singular limit ($\tau \rightarrow 0$), moisture abruptly changes the characteristic properties of the model and the boundary between nonprecipitating and precipitating regions appears as the intersection between dry and moist characteristics.

Note that the system is not necessarily piecewise hyperbolic, its type depending on the values of parameters. If h

$-\beta Q_s < 0$, $c^m - u$ is imaginary and the system becomes piecewise elliptic/hyperbolic for $\tau \rightarrow 0$. Such a system has been studied in Ref. 34.

D. Fronts propagation and Rankine–Hugoniot conditions

In this subsection we analyze the propagation of discontinuities (fronts) in MC-RSW and, in particular, the precipitation fronts which delimit precipitating and nonprecipitating regions. Propagating discontinuities represent *weak solutions* of the hyperbolic system which must satisfy RH jump conditions. These conditions are obtained from the equations of the system rewritten in the form of mass and momentum conservation laws (e.g., Ref. 33).

1. The nature of the discontinuities

The 1.5D MC-RSW equations inherit from the parent RSW model a capability to form strong shocks (i.e., discontinuities in u and h at continuous v) and contact discontinuities (i.e., discontinuities in v at continuous u, h), see Refs. 35 and 36. Indeed at finite relaxation time, P is a continuous function of Q and does not contain derivatives. Hence it does not contribute to the RH conditions because in the integrated equations (serving to deduce the RH conditions),

$$\lim_{a \rightarrow x_s^-} \lim_{b \rightarrow x_s^+} \int_a^b P dx = 0, \quad (2.32)$$

where x_s is the position of a discontinuity. The corresponding RH conditions for the hydrodynamic sector may be found, e.g., in Ref. 36,

$$\begin{aligned} -s[hu] + [hu^2 + \frac{1}{2}gh^2] &= 0, \\ -s[hv] + [huv] &= 0, \\ -s[h] + [hu] &= 0, \end{aligned} \quad (2.33)$$

where s is the speed of the discontinuity and $[\dots]$ is the jump of any quantity across the discontinuity. As usual, the speed of a strong discontinuity (shock) is close to the “sound” velocity, i.e., the velocity of the short inertia-gravity waves \sqrt{gh} ,

$$(u_- - s)^2 = g \frac{h_- + h_+}{2} \frac{h_+}{h_-}, \quad (2.34)$$

where the indices $+$ ($-$) denote the values on the right (left) of the discontinuity. It is easy to see that adding a discontinuity in Q and the corresponding jump condition,

$$-s[Q] + [Qu] = 0, \quad (2.35)$$

does not change this analysis. Similarly, at a contact discontinuity moving with a local speed $s=u$ the tangential velocity v and humidity Q can have arbitrary jumps, while u and h are continuous. However, it is worth noting that a jump in Q uniquely determines a jump in the derivative of velocity. Indeed, by differentiating the equations for u and h we get

$$\partial_x u + \partial_x (u \partial_x u + g \partial_x h) = f \partial_x v, \quad (2.36)$$

$$\partial_{tx}h + \partial_x(h\partial_xu + u\partial_xh) = -\beta\partial_xP, \quad (2.37)$$

giving the RH conditions,

$$(u-s)[\partial_xu] + g[\partial_xh] = 0, \quad (2.38)$$

$$(u-s)[\partial_xh] + h[\partial_xu] = -\beta[P]. \quad (2.39)$$

Now, P is a continuous function of Q and, thus, inherits its jump. Therefore, for a contact discontinuity with $s=u$ we get

$$[\partial_xh] = 0, \quad h[\partial_xu] = -\beta[P]. \quad (2.40)$$

Hence, we see that jumps in P , i.e., *precipitation fronts*, are related to jumps in derivatives of dynamical variables, i.e., *weak discontinuities*. This fact was already emphasized in Ref. 6 where, by using the energy principle and the linearization of the hydrodynamical sector, it was shown that smooth initial conditions cannot develop discontinuities in the dynamical variables, but discontinuities in the gradients of these variables only.

Note also that for immediate relaxation ($\tau \rightarrow 0$), integral (2.32) also vanishes except for an eventual discontinuity point x_s inside a precipitating region $P = -Q_s\partial_xu > 0$. In this special case, the RH conditions are given by

$$-s[u] + \frac{1}{2}[u^2] + g[h] = 0, \quad (2.41)$$

$$-s[h] + [uh] - \beta Q_s[u] = 0. \quad (2.42)$$

2. Weak discontinuities and the speed of fronts

Following Frierson *et al.*,⁶ we proceed below with the analogous analysis for the MC-RSW model. By adding to Eqs. (2.36) and (2.37) the equation for the gradient of moisture,

$$\partial_{tx}Q + \partial_x(Q\partial_xu + u\partial_xQ) = -\partial_xP, \quad (2.43)$$

we can straightforwardly obtain the corresponding jump equation

$$(u-s)[\partial_xQ] + Q[\partial_xu] = -[P] \quad (2.44)$$

and get a full system of RH conditions for the gradients of the 1.5D MC-RSW. No strong discontinuity is supposed in the variables $\{u, h, Q\}$ and the equation

$$(u-s)[\partial_xv] = 0 \quad (2.45)$$

is supposed to be satisfied by $[\partial_xv]=0$, in order to eliminate trivial solutions $s=u$.

For *finite relaxation time* ($\tau \neq 0$), there is no discontinuity in P because it is a function of Q , which is supposed to be continuous: $[P]=0$. Thus, three solutions for s can be found with the values of the characteristic velocity (2.21). We call them *nonprecipitating fronts*, as their speed does not depend on humidity.

For *immediate relaxation*, the jump in P can be expressed as $[P]=P_+ - P_- = -Q_s(\partial_xu)_+ > 0$ with the choice $(\partial_xu)_+ < 0$ [see Eq. (2.24)] and $P_- = 0$, where the precipitating (nonprecipitating) regions are denoted by $+$ ($-$). Since $[\partial_xQ] < 0$ and $Q=Q_s$ at the interface, Eqs. (2.38), (2.39), and (2.44) can be rewritten as follows:

$$[\partial_xu]\{(u-s)^2 - gh\} = g\beta[P], \quad (2.46)$$

$$[\partial_xu]\left\{(u-s) - \frac{gh}{(u-s)}\left(1 - \frac{\beta Q_s}{h}\right)\right\} = -g\beta[\partial_xQ],$$

and three different types of solutions—the precipitation fronts—can exist:

- (1) the dry subsonic fronts, $c_m < \hat{s} < c_d$,
- (2) the moist subsonic fronts, $-c_m < \hat{s} < 0$, and
- (3) the moist supersonic fronts, $\hat{s} < -c_d$,

where $\hat{s}=s-u$ is the relative front velocity and (c_d, c_m) are the dry and moist speeds described in Sec. II D 1. Note that $\hat{s} \rightarrow -\hat{s}$ if precipitating and nonprecipitating regions are inverted: $[P] < 0$ and $[\partial_xQ] > 0$. Such fronts are nonlinear analogs of the precipitation fronts found in Ref. 6. We should stress that only the dry subsonic fronts satisfy the Lax stability criterion: The shock is *compressive* if the characteristic velocity behind it ($c_d > \hat{s}$) is higher than the characteristic velocity in front of it ($\hat{s} > c_m$). Yet, we were able to reproduce all types of fronts numerically—see Sec. III. At this point it is important to remind that information is transmitted along the characteristics, and not by shocks (fronts), which are the result of intersections of characteristics. This explains why supersonic fronts are observable. Note that scattering of simple waves in the context of immediate relaxation can be understood as scattering by precipitation fronts, as discussed in detail in Ref. 7.

III. NUMERICAL EXPERIMENTS

A. Choice of parameters

In order to make numerical simulations with the MC-RSW model, we use a second-order finite-volume method developed by Bouchut.²⁰ The method is efficient, well balanced, treats extremely well topography and Coriolis force (although these properties are not of utmost importance for the numerical experiments presented below, they are crucial for further, more realistic simulations), and is extensively tested in the geophysical fluid dynamics context (e.g., Ref. 37). In addition, numerical implementation of the Betts–Miller-type scheme is straightforward (see Appendix C).

In the experiments presented below we work with the “equatorial” (cf. Ref. 6) 1D version of the model setting $f=0$ and $v(x,0)=0$. The nondimensional horizontal scale of the domain is fixed at $L_x \times L_y = 12 \times 12$ in the units of length L . Since there is no intrinsic horizontal scale in the model without rotation, the length scale is $L = \sqrt{gH_0T}$, where H_0 is the layer thickness at rest and T is the unit of time (e.g., the synoptic scale $L \approx 1000$ km can be achieved for $H_0 \approx 5$ km and $T \approx 1$ h).

We choose a grid of high resolution in the zonal direction x ($n_x \geq 1000$ points). The time step is chosen as the minimum between a specific value allowing to respect the Courant–Friedrich–Levy condition, Δt^{CFL} , and an arbitrary chosen maximum value $\Delta t^{\text{max}} = 2 \times 10^{-3}$.

We use Neumann boundary conditions which are numerically implemented by requiring that each variable has the same values in the first two and last two cells of the

domain. These boundary conditions do not forbid complex reflections of the solutions and numerical dissipation at the boundaries. Nonetheless, these effects are weak far from the boundaries and do not affect our simulations (see below).

The precipitation term is parametrized by Eq. (2.8)—see Appendix C. The relaxation time is linked to the time step of the numerical scheme,

$$\tau = \gamma \Delta t, \quad (3.1)$$

which allows us to control the relaxation by varying the parameter γ . Thus, “immediate” relaxation corresponds to $\gamma = 1$ and slow relaxation to $\gamma \gg 1$. It is however important to keep in mind that numerical instabilities do not allow to take γ too small (precipitation being a stiff source), and thus numerically the relaxation is never immediate but just fast.

The system is scaled in a way that the dry characteristic velocity in the linear limit equals unity, $c_d = \sqrt{gH_0} = 1$, and we choose the following values for parameters:

$$g = 1 \quad \text{and} \quad H_0 = 1. \quad (3.2)$$

The observations in the real atmosphere show that the moist characteristic velocity values are $c_m \approx 0.3c_d$.³⁸ For $\beta = 1$, we therefore choose $Q_s = (1 - c_m^2) = 0.9$, which corresponds to the value used by Majda and co-workers^{6,7,18} in most of their numerical experiments with the linearized model.

B. Experiment 1: Scattering of a simple wave by a moisture front

In the first experiment our numerical scheme is benchmarked against analytic results and, at the same time, some typical dynamical effects of moisture are illustrated. A localized simple wave solution, well known in gas dynamics (e.g., Ref. 33), was chosen as initial configuration and launched in the direction of a moisture front. This is an idealized model of a situation where a large-scale tropical perturbation encounters a quasisaturated area. The interaction of the incoming localized perturbation with the moisture front can create an area of precipitation and modify the properties of characteristics.

1. Initial conditions: Simple wave and moisture front

A simple wave is a solution which propagates along a single characteristic. To obtain it, the initial condition must be chosen to cancel one of the propagating Riemann variables. In the linear limit and for $\tau \neq 0$, the Riemann variables for perturbations are given by

$$\rho_q = q - \frac{Q_s}{H_0} \eta, \quad (3.3)$$

$$\rho_{\pm} = u \pm \sqrt{\frac{g}{H_0}} \eta, \quad (3.4)$$

where $\{u, \eta, q\}$ is a small perturbation over the state of rest $\{0, H_0, Q_s\}$. An eastward-propagating simple wave is then obtained by imposing the condition

$$\rho_- = 0 \quad (3.5)$$

(equivalently $\rho_+ = 0$ for a westward-propagating simple wave).

Initially stationary moisture front is taken in the form

$$Q(x, 0) = Q_s [1 + q_0 \tanh(x - x_M) H(-x + x_M)], \quad (3.6)$$

where $x_M = 6$ is the middle of the domain and $q_0 = 0.05$ is the amplitude of the moisture jump. We choose

$$u(x, 0) = \mu(x) \quad \text{and} \quad h(x, 0) = H_0 + \sqrt{\frac{H_0}{g}} \mu(x), \quad (3.7)$$

and a localized parabolic spatial profile

$$\mu(x) = \alpha [- (x - x_p)^2 + \epsilon] H(x - x_p + \sqrt{\epsilon}) H(-x + x_p + \sqrt{\epsilon}), \quad (3.8)$$

where $\alpha = \pm 1$, x_p is the initial position of the simple wave, and $\epsilon = 0.025$ determines the amplitude and the width of the perturbation. The amplitude of the wave was deliberately taken to be small for the sake of comparison with the linear theory of Refs. 6, 7, 17, and 18.

The simple wave is chosen to start from the unsaturated region ($x_p = 2$), with convergence at its eastern side ($\alpha = +1$) such that it triggers precipitation near the moisture front. The relaxation time is fixed by $\gamma = 5$ and the saturation level is $Q_s = 0.9$.

2. Numerical results

In the unsaturated region it is expected from the theory that the solution propagates along the dry characteristic with velocity $c_d = 1$. On its way, it makes the humidity field q grow and then decrease. Since the wave is symmetric, the two effects cancel each other and the net effect is just a modulation of the humidity field (except for $t = 0$). As long as moisture is not saturated ($t < 3.4$), these predictions are well reproduced by the numerical model, as shown by the Hovmöller (characteristic) diagrams of humidity Q and velocity u (Fig. 2). Note that the characteristics in the dry region are straight because of the smallness of the initial perturbation.

When the simple wave approaches the moisture front, the saturation is reached (near $t \approx 3.4$) and a precipitating region appears (Fig. 3). For finite relaxation time ($\gamma > 0$), precipitation modifies the Riemann variables: The eastward-propagating simple wave, $\rho_+(x, t)$, is progressively destroyed, while a westward-propagating simple wave $\rho_-(x, t)$ appears. This process ends when precipitation stops ($t \approx 4.6$). As is clear from Fig. 2, the precipitation leads to *reflection* of the eastward-moving disturbance at the moisture front, which is accompanied by a weak displacement and smoothening of the front. As shown in Fig. 4, the total energy E decreases in time during this process which confirms that the energy budget of the model is consistent with Eq. (2.13).

The specific form of the precipitating region observed in Fig. 3 may be understood on the basis of the immediate relaxation approximation phenomenology, which is not out of place here as the relaxation time with $\gamma = 5$ is still of the order of the time step of the model and thus very fast. In fact,

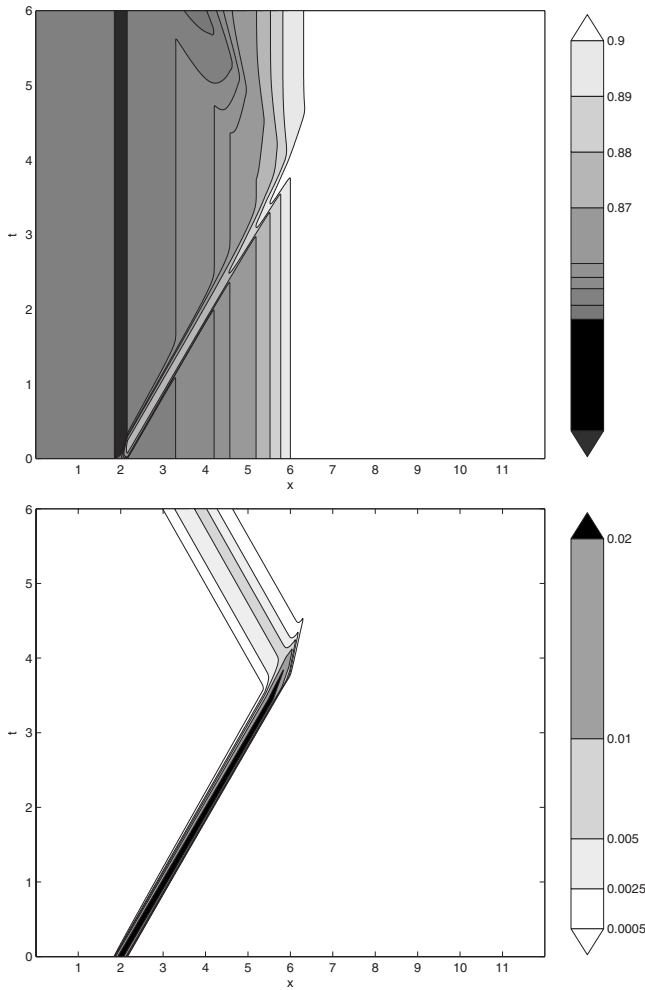


FIG. 2. Hovmöller diagrams of the humidity field $Q(x,t)$ (upper panel) and the velocity field $u(x,t)$ (lower panel). A parabolic eastward-propagating simple wave ($\alpha=+1$, $\epsilon=0.025$) initially centered in the unsaturated region ($x_p=2$, $Q_s=0.9$) propagates along its dry characteristic ($c_d=1$) and interacts with a moisture front ($x_M=6$). It is destroyed by precipitation and a westward-propagating simple wave emerges. $\gamma=5$, $n_x=1500$. The dark vertical line on the upper panel corresponds to a characteristic with zero velocity related to humidity, cf. Eq. (2.18).

this region arises in front of the moisture front ($x < x_M=6$) due to nonlinear precipitation term. It is delimited by two precipitation fronts. The western side corresponds to a *dry subsonic front* ($c_m < s_1 \approx 0.7 < c_d$) for which the jump configuration is given by

$$[\partial_x u] < 0, \quad [\partial_x q] < 0, \quad \text{and} \quad [P] > 0, \quad (3.9)$$

where $[a]=a_+ - a_-$, $(-/+)$ denoting the western/eastern side. The eastern side appears as a *moist supersonic front* ($s_2 \approx 1.2 > c_d$) in the following jump configuration:

$$[\partial_x u] < 0, \quad [\partial_x q] < 0, \quad \text{and} \quad [P] < 0. \quad (3.10)$$

The lifetime of these fronts depends on the time of existence of the discontinuity in the humidity gradient $\partial_x q$. This is clearly seen for the moist supersonic front which disappears at the initial moisture front ($x_M=6$), where the humidity becomes saturated: $q_+=0$ and $(\partial_x q)_+=0$. In the dry subsonic front case, it persists through the moisture front due to the wind divergence, $(\partial_x u)_- > 0$, that continues to dry out the

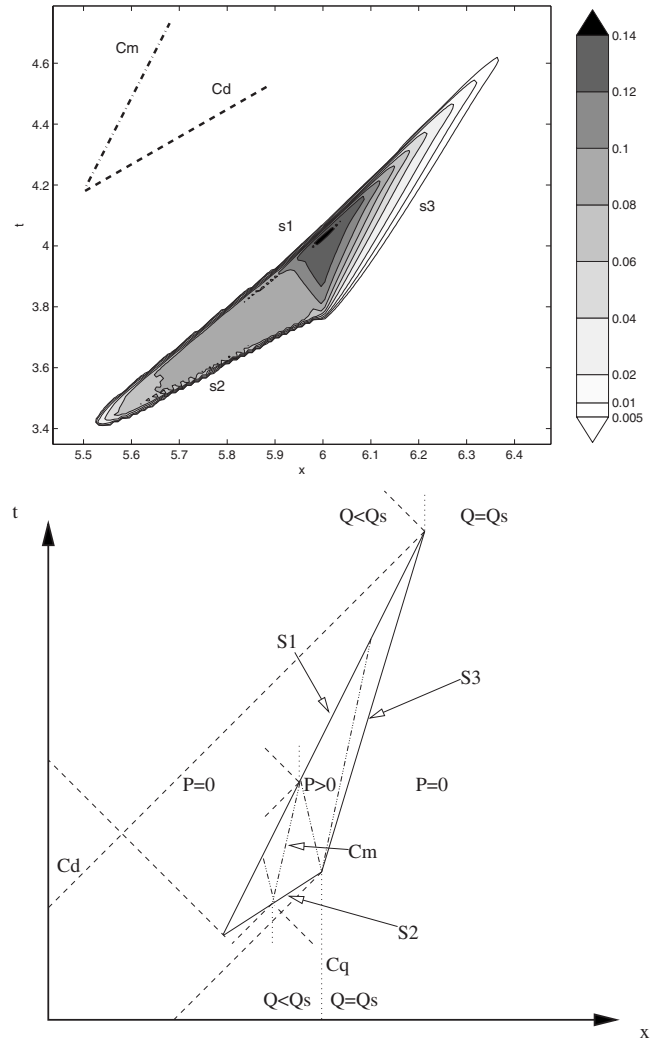


FIG. 3. Same experiment as Fig. 2. Precipitation $P(x,t)$ zoomed in the interaction area (upper panel) and corresponding sketch of characteristics (lower panel). Precipitating region is delimited by a dry subsonic ($s_1 \approx 0.7$) and a moist supersonic precipitation front ($s_2 \approx 1.2$) obtained in the approximation of immediate relaxation. The third limiting line (s_3) can be viewed as the last ($\partial_x u \rightarrow 0$) eastward-propagating moist characteristic (3.11) of the gradient system for a quasi-immediate relaxation. In the lower panel, the limits of the precipitating region (s_1, s_2, s_3) are denoted by solid lines, the dry (moist) characteristics c_d (c_m) by dashed (dashed-dotted) lines, and the characteristic c_q by dotted lines.

layer and maintains the jump $[\partial_x q] < 0$ until the end of precipitation.

Along the same lines, we can test the manifestations of the moist characteristics in the precipitating region. Figure 5 shows the Hovmöller diagrams of the moist Riemann variables r_{\pm}^m [Eq. (2.29)] for the same simulation. The associated moist characteristics of velocity $c_m \approx 0.3$ can be indeed seen in the precipitating region, as suggested by Eqs. (2.27) and (2.28).

The third limiting line of the precipitating region in Fig. 3 corresponds to a velocity between the dry and the moist ones: $c_m < s_3 < c_d$. Strictly speaking, this is not a front. It can be viewed as the “last” eastward-propagating moist characteristic. Precisely, in the saturated region $Q=Q_s$, with no wind divergence ($\partial_x u \leq 0$), precipitation becomes param-

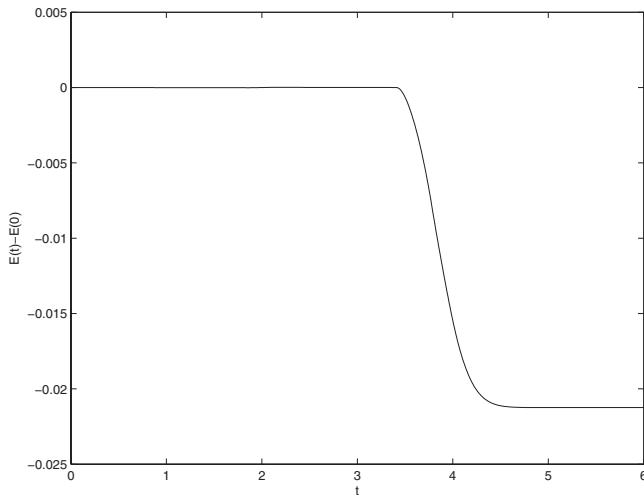


FIG. 4. Time evolution of the energy variation $[E(t) - E(0)]$ corresponding to Fig. 2. Dissipation by precipitation takes place during the interaction between an eastward-propagating simple wave and a moisture front.

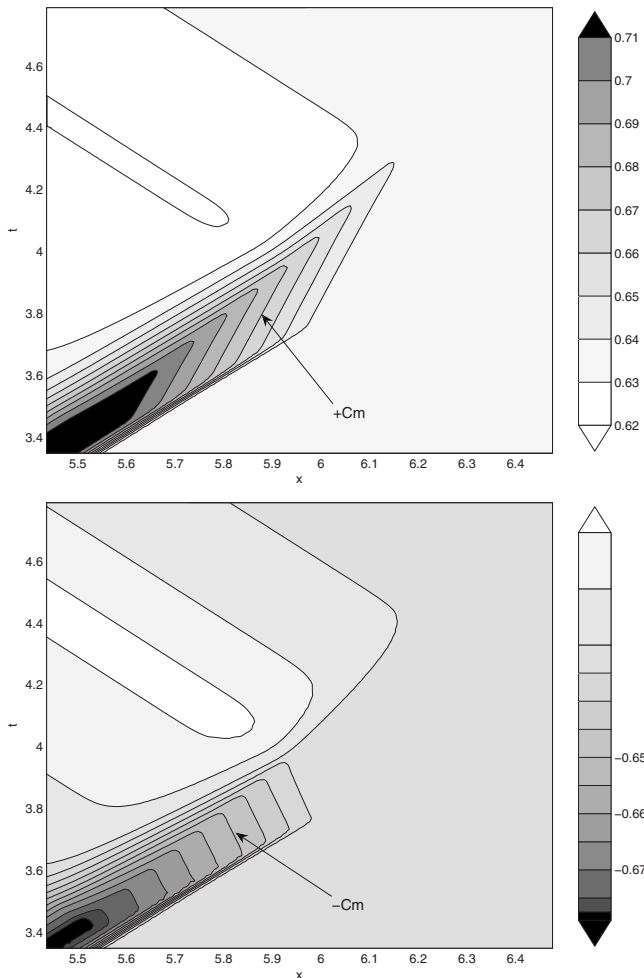


FIG. 5. Hovmöller diagrams of the eastward- and westward-propagating moist Riemann variables: $r_+^m(x, t)$ (upper panel) and $r_-^m(x, t)$ (lower panel) zoomed in the interaction area. For rapid relaxation with $\gamma=5$, these variables display the moist characteristic ($c_m \approx 0.3$) in the precipitating region corresponding to Fig. 3. Same simulation as in Fig. 2.

etrized by $P = -Q_s \partial_x u H(-\partial_x u) \geq 0$ for $\tau \rightarrow 0$. In this case, the gradient systems (2.36) and (2.37) become totally hyperbolic. If we consider a *quasi-immediate* relaxation approximation, we can replace the Heaviside function by a regularized one $H_\delta(\cdot)$ such that $H_{\delta \rightarrow 0}(\cdot) = H(\cdot)$. Then, one can show that the speed of the eastward-propagating characteristic of the gradients system (for linearized hydrodynamic part) depends on the wind convergence value ($\partial_x u < 0$),

$$c_+ = \sqrt{g[H_0 - \beta Q_s H_\delta(-\partial_x u)]}. \tag{3.11}$$

This speed increases when wind convergence decreases. The third limiting line s_3 is then the print of the last of these moist characteristics in the sense that this is the boundary between characteristics where convergence and precipitation still occur but tend to zero, $\{\partial_x u, P\} \rightarrow 0$ and characteristics which become strictly dry ($c_+ = c_d$) for $\partial_x u = 0$ ($P = 0$).

This analysis of the interaction area between the simple wave and the moisture front is completed by the sketch of the dry and moist characteristics and of the limits of the precipitating region presented in the lower panel of Fig. 3.

The same experiment was performed with a different choice of the relaxation time $\gamma = 100$. In this case, the relaxation is slow and no precipitation fronts nor moist characteristics are expected. The corresponding Hovmöller diagrams of the velocity field u and precipitation P are shown in Fig. 6. We observe the same reflection process which, however, lasts longer than in the previous experiment. The precipitating region is deformed with respect to Fig. 3 but still keeps track of fronts which are smoother, the higher the value of γ . The moist characteristics are not visible anymore in the diagrams of moist Riemann variables (compare Fig. 7 to Fig. 5).

The configuration with an eastward-propagating simple wave of the opposite sign ($\alpha = -1$), with wind divergence at its eastern side, can be also studied. In that case, no reflected wave was observed but when the simple wave approaches the moisture front, it starts *drying* (not shown). For a perfectly symmetric wave a modulation in the humidity field along its trajectory with no precipitation would be found (not shown).

C. Experiment 2: Evolution of a perturbation in a saturated region

We present below another type of numerical experiment which is also directly comparable to analytical results consisting of the propagation of a small perturbation through a uniformly saturated region, as in Ref. 17.

1. Initial conditions

We choose a Gaussian perturbation of the velocity field $u(x, 0)$, which propagates into a uniformly saturated region $Q(x, 0) = Q_s$ at rest,

$$h(x, 0) = H_0, \quad u(x, 0) = \mu(x) = \mu_0 \exp\left(\frac{-(x - x_M)^2}{2}\right). \tag{3.12}$$

In order to make connection with the linear theory the amplitude is fixed to be small: $\mu_0 = 0.025 > 0$.

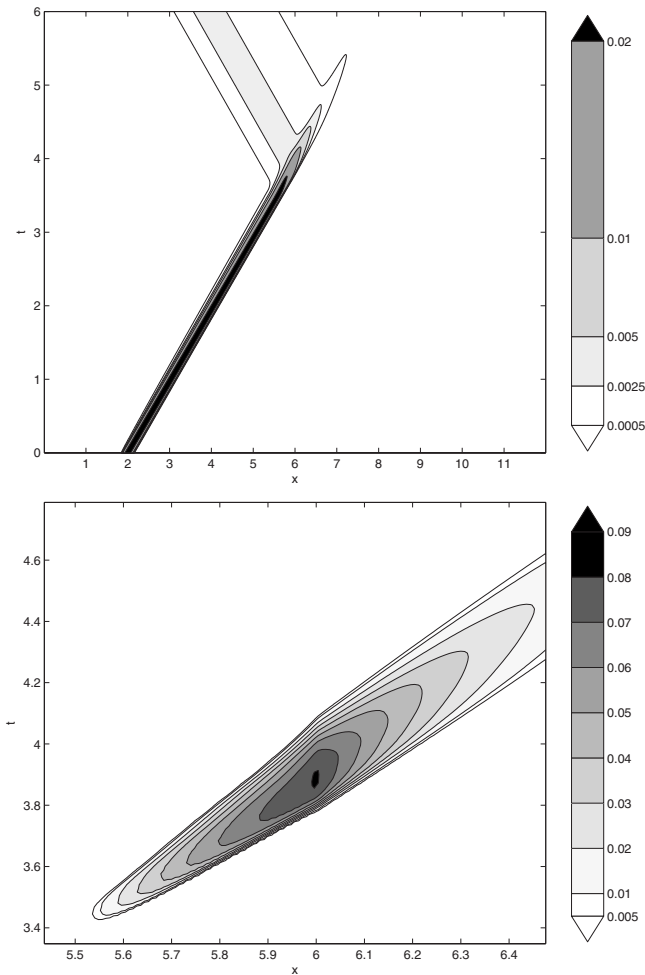


FIG. 6. Same experiment as in Fig. 2 but for slow relaxation $\gamma=100$. Velocity field (upper panel) and precipitation (lower panel). Lower panel shows the same zoom as in upper panel of Fig. 3.

This type of initial condition can be treated analytically by the method of characteristics for $\tau \rightarrow 0$. Starting from gradient systems (2.36), (2.37), and (2.43) and its linearized dry and moist Riemann variables, we can follow the evolution of the disturbance and identify the precipitation front formation by the pattern of the intersection of characteristics. A problem of *a priori* identification of the precipitation regions however arises, as this kind of initial conditions is degenerate, and the characteristics are not defined for $\tau=0$. To solve it, we perform a Taylor expansion in time of the linearized equations at $\tau \neq 0$. At the first two orders the evolution of the humidity perturbation $q=Q-Q_s$ is given by

$$\begin{aligned}
 q(x, \Delta t) &\approx q(x, 0) \\
 &+ \left\{ -Q_s \partial_x u(x, 0) - (1 + Q_s) \frac{q(x, 0)}{\tau} H[q(x, 0)] \right\} \Delta t \\
 &+ \left\{ \frac{Q_s}{2} \partial_{xx} \eta(x, 0) - (1 + Q_s) \frac{\partial_t q(x, 0)}{\tau} H[q(x, 0)] \right\} \Delta t^2.
 \end{aligned} \tag{3.13}$$

Thus, for $q(x, 0)=0$ and $\eta(x, 0)=0$ the perturbation is deter-

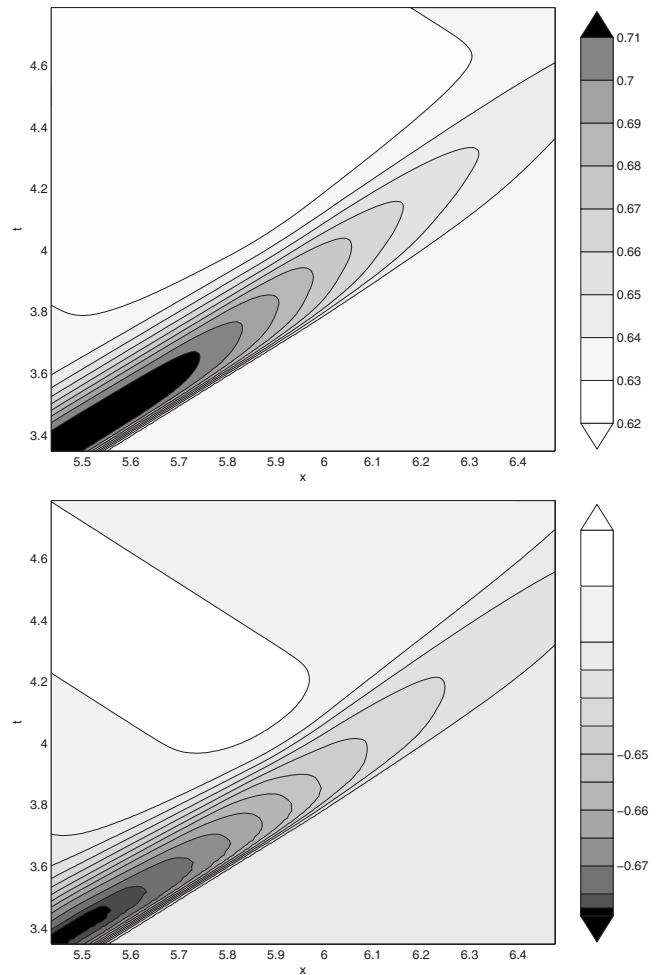


FIG. 7. Same as in Fig. 5 but for slow relaxation $\gamma=100$. Moist characteristics are not visible anymore in the precipitating region.

mined by $\partial_x u(x, 0)$ and is independent of τ at the first order. We therefore deduce from Eq. (3.12) that $P=0$ for $x < x_M$ and $P > 0$ for $x > x_M$.

2. Front formation

The gradient systems (2.36), (2.37), and (2.43) can be linearized in the hydrodynamic sector and rewritten in the characteristic form in the limit $\tau \rightarrow 0$. In the nonprecipitating region, we thus have

$$\frac{d}{dt} R_{\pm}^d = \frac{d}{dt} (g \partial_x \eta \pm c_d \partial_x u) = 0 \quad \text{on} \quad \frac{dx}{dt} = \pm c_d, \tag{3.14}$$

$$\frac{d}{dt} R_0^d = \frac{d}{dt} \left(\partial_x q - \frac{Q_s}{H_0} \partial_x \eta \right) = 0 \quad \text{on} \quad \frac{dx}{dt} = 0, \tag{3.15}$$

where $c_d = \sqrt{gH_0}$. In the precipitating region, we have

$$\frac{d}{dt} R_{\pm}^m = \frac{d}{dt} (g \partial_x \eta \pm c_m \partial_x u) = 0 \quad \text{on} \quad \frac{dx}{dt} = \pm c_m, \tag{3.16}$$

where $c_m = \sqrt{g(H_0 - \beta Q_s)}$. Note that the associated Riemann invariants $\{R^d, R^m\}$ are just proportional to the derivative of the linearized version of the Riemann variables described in Eqs. (2.20) and (2.29), e.g., in the nonprecipitating region:

$R_0^d = \partial_x \rho_q$ and $R_{\pm}^d = \pm c_d \partial_x \rho_{\pm}$ from Eqs. (3.3) and (3.4).

The initial conditions allow to partially determine the Riemann invariants in each region. For $x < x_M$,

$$R_+^d(x) = -R_-^d(x) = c_d \partial_x \mu(x) \quad \text{and} \quad R_0^d(x) = 0, \quad (3.17)$$

and for $x > x_M$,

$$R_+^m(x) = -R_-^m(x) = c_m \partial_x \mu(x). \quad (3.18)$$

At the boundary point $x = \xi(t)$ where the characteristics intersect each other, we can have either *continuous* or *discontinuous* spatial gradients.

3. The continuity condition

Because the initial condition is smooth in $\xi(0) = x_M$, let us suppose first the continuity of gradients,

$$\lim_{x \rightarrow \xi^-} \partial_x u[\xi(t), t] = \lim_{x \rightarrow \xi^+} \partial_x u[\xi(t), t] = 0. \quad (3.19)$$

In terms of Riemann invariants we obtain

$$\begin{aligned} & \frac{R_+^d[\xi(t) - c_d t] - R_-^d[\xi(t) + c_d t]}{c_d} \\ &= \frac{R_+^m[\xi(t) - c_m t] - R_-^m[\xi(t) + c_m t]}{c_m} \\ &= 0, \end{aligned} \quad (3.20)$$

with analogous condition on $\partial_x \eta[\xi(t), t]$,

$$\begin{aligned} & R_+^d[\xi(t) - c_d t] + R_-^d[\xi(t) + c_d t] \\ &= R_+^m[\xi(t) - c_m t] + R_-^m[\xi(t) + c_m t]. \end{aligned} \quad (3.21)$$

If the motion of the boundary obeys the inequality $-c_m t < (\xi(t) - x_M) < c_d t$, we get from the initial conditions the *continuity condition*,

$$c_d \partial_x \mu[\xi(t) - c_d t] + c_m \partial_x \mu[\xi(t) + c_m t] = 0. \quad (3.22)$$

The equation for the boundary velocity $d\xi/dt$ can be found by differentiating the continuity condition. Equation (3.22) is verified at the initial time $t=0$ for the Gaussian profile of the perturbation $\mu(x)$. However, it is an implicit equation for the position of the boundary $\xi(t)$ and cannot be solved analytically in general.

We can, nevertheless, find criteria of violation of the continuity condition. Indeed, the boundary velocity cannot exceed the velocity of characteristics that emerge from and in front of the boundary itself, otherwise the intersection of the characteristics changes, and a shock in the gradients occurs. This is shown in the sketch of Fig. 8 which describes the characteristics for the continuity condition (upper panel) and for a shock (lower panel). The latter appears when the boundary moves faster than the moist Riemann variables R_+^m : $d\xi/dt > c_m$.

The initial velocity of the boundary can be determined by using the first order Taylor expansion in time of the continuity condition,

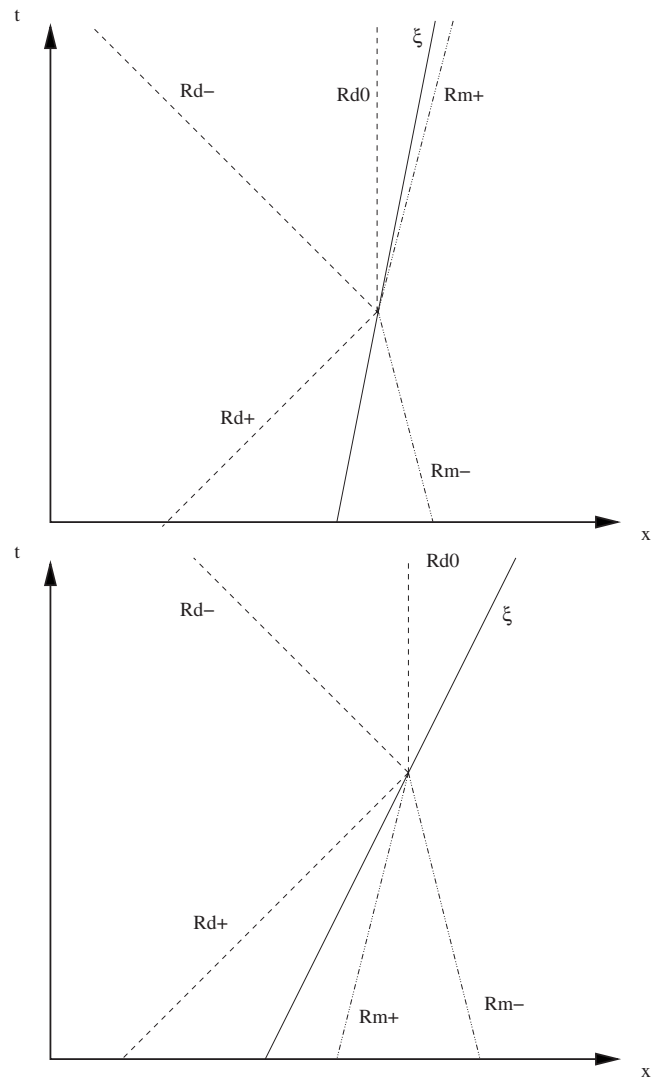


FIG. 8. Sketch showing the characteristics for continuity condition (upper panel) and jump condition (lower panel) for gradients at the boundary $\xi(t)$ between precipitating and nonprecipitating regions in the limit of immediate relaxation for infinitesimal disturbances. Dry (moist) characteristics are denoted by dashed (dashed-dotted) lines and the boundary by a solid line.

$$\left. \frac{d\xi}{dt} \right|_{t=0} = c_d - c_m > 0. \quad (3.23)$$

Hence, a criterion of immediate shock formation in the velocity gradient $\partial_x u$ is

$$c_d - c_m > c_m \Rightarrow Q_s > \frac{3H_0}{4\beta}. \quad (3.24)$$

We should stress that this condition on Q_s is different from the one obtained in Ref. 17 because of the different choices of initial disturbance [in Ref. 17, $u(x,0)=0$ and $h(x,0)=H_0 - \Theta(x)$, where $\Theta(x)$ is monotonic increasing and antisymmetric about x_M]. By the same method, a simple expression of the boundary speed for the continuity condition for all times, $d\xi/dt = (c_d - c_m)/2$, and the resulting criteria of immediate shock formation, $Q_s > 8H_0/9\beta$, were found in Ref. 17.

4. Jump condition

If a jump in the gradients occurs at the boundary $\xi(t)$, it is a precipitation front and it has to satisfy the linearized version of RH conditions (2.38), (2.39), and (2.44). If the boundary velocity exceeds the moist characteristic velocity, $d\xi/dt > c_m$, the boundary cannot be defined by the condition $\partial_x u[\xi(t), t] = 0$ anymore. It rather corresponds to the position of a dry subsonic front,

$$(\partial_x u)[\xi(t), t] \neq 0, \quad \text{with} \quad c_m < s = \frac{d\xi}{dt} < c_d. \quad (3.25)$$

It is possible to express the front velocity in terms of Riemann invariants,⁷

$$s = \frac{c_m(c_d + c_m)R_+^m + c_m(c_d - c_m)R_-^m - 2c_m c_d R_+^d}{(c_d + c_m)R_+^m - (c_d - c_m)R_-^m - 2c_m R_+^d}. \quad (3.26)$$

Since Riemann invariants themselves depend on $\xi(t)$, one has to solve the implicit equation,

$$\begin{aligned} \mathcal{F}[\xi(t), s(t), t] \equiv & (s - c_m)(c_d + c_m)\partial_x \mu(\xi - c_m t) \\ & + (s + c_m)(c_d - c_m)\partial_x \mu(\xi + c_m t) \\ & - 2(s - c_d)c_d \partial_x \mu(\xi - c_d t) \\ = & 0, \end{aligned} \quad (3.27)$$

in order to find $s(t)$. When a shock appears immediately ($Q_s > 3H_0/4\beta$), a Taylor expansion in time of this equation gives the initial front velocity which is independent of Q_s : $s(0) = c_d/2$. This value still depends on the choice of initial conditions and differs from the one obtained in Ref. 17: $s(0) = c_d/3$.

5. Numerical results

The theory described above can be directly compared to numerical results. We set a rapid relaxation by taking $\gamma = 5$ as in the previous experiment. Two sets of simulations were performed with different saturation values Q_s .

In the first one, we chose $Q_s = 0.7$, such as $Q_s < 3/4$ and continuity condition was initially satisfied. As shown by the Hovmöller diagrams of the velocity gradient field $\partial_x u$ and the precipitation P (Fig. 9), the boundary $\xi(t)$ starts propagating following the continuity condition. Its velocity increases with time and no shock appears as long as the velocity is weaker than the moist velocity. After $t \approx 1.5$, we can distinguish a front (which is already seen at $t \approx 1$ in the spatial profiles, not shown). This is a dry subsonic precipitation front with velocity increasing with time.

We also solve numerically the implicit Eqs. (3.22) and (3.27) defining the boundary evolution $\xi(t)$ from the continuity and jump conditions. For the first equation, we use the initial conditions found by the Taylor expansion given above: $\xi(0) = x_M$ and

$$\left. \frac{d\xi}{dt} \right|_{t=0} = c_d - c_m \approx 0.4523, \quad (3.28)$$

while for the second, we need to determine the time t_s , when the boundary velocity exceeds the moist velocity $c_m \approx 0.5477$ from the resolution of the first equation. We then

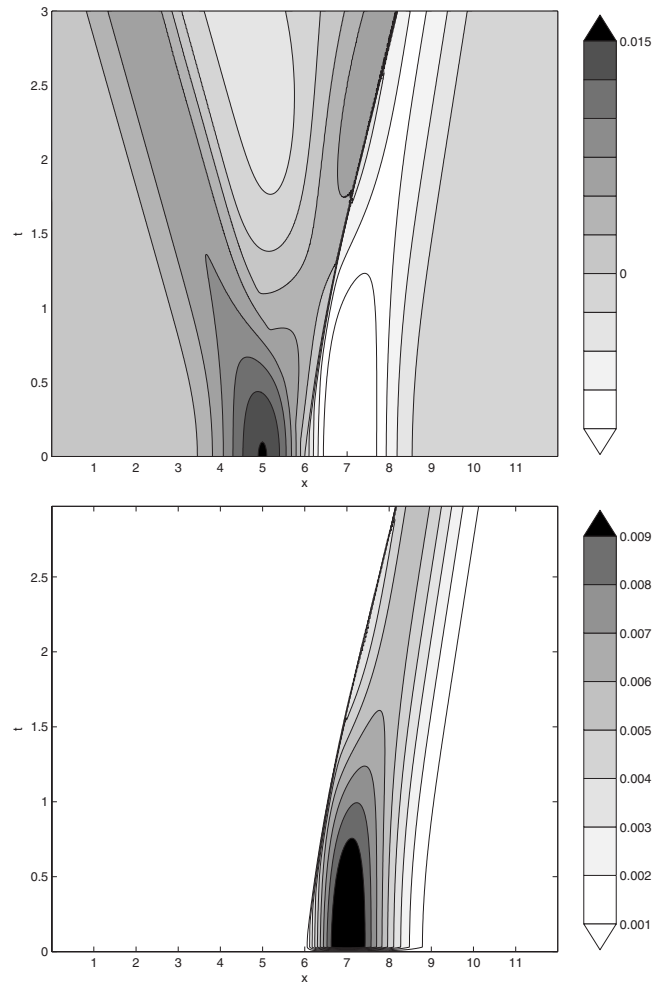


FIG. 9. Hovmöller diagrams of the velocity gradient field $\partial_x u(x, t)$ (upper panel) and precipitation $P(x, t)$ (lower panel) for a small Gaussian disturbance in velocity ($\mu_0 = 0.025$) propagating into a saturated domain ($Q_s = 0.7$), and creating precipitating and nonprecipitating regions. In the immediate relaxation limit, the boundary $x = \xi(t)$ between these two regions corresponds to the intersection of dry and moist characteristics. Initially the gradients are continuous at $\xi(t)$: This can be interpreted as a smooth precipitation front. When boundary velocity exceeds the moist velocity $c_m \approx 0.5477$, a dry subsonic precipitation front emerges. It is well identified for $t > 1.5$ in this figure. $\gamma = 5$ and $n_x = 1500$.

use the values $\xi(t_s)$ and $s(t_s)$ as initial conditions. The two alternative boundary evolutions thus obtained are compared to the result of the DNS in Fig. 10. A good agreement between analytical and the DNS results is observed. The continuity condition coincides with the boundary evolution curve of the DNS until $t \approx 0.75$, and then detaches while the shock condition starts for $t_s \approx 0.3$ and closely follows the DNS.

For higher saturation values, such as $Q_s > 3/4$, a dry subsonic precipitation front immediately arises. The results of the numerical experiment with $Q_s = 0.95$ are shown in Fig. 11. The implicit equation for shock condition (3.27) was also solved, starting from the initial conditions found above: $\xi(0)$, $s(0) = 1/2$, and the analytical and DNS results for boundary evolution are still in good agreement, as shown in Fig. 12.

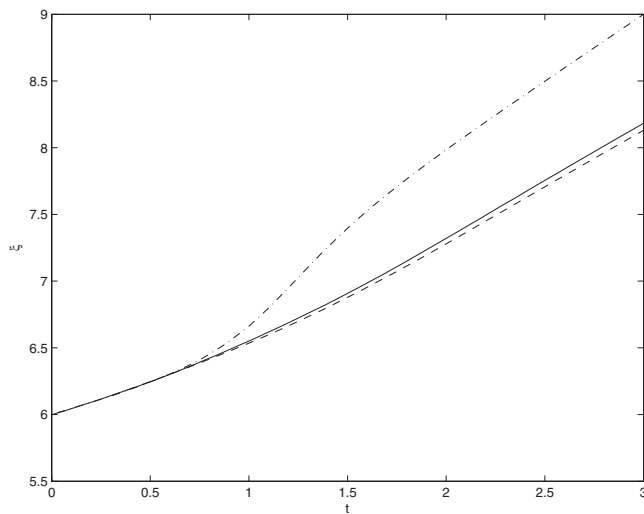


FIG. 10. Evolution of the position of the boundary $\xi(t)$ between precipitating and nonprecipitating regions. The boundary is created by a Gaussian disturbance in the velocity field ($\mu_0=0.025$) which propagates into a saturated domain ($Q_s=0.7$). The DNS result (solid) is compared to the solutions of the implicit equations for continuity (dashed-dotted) and shock condition (dashed). $\gamma=5$ and $n_x=7500$ for the DNS.

D. Experiment 3: Nonlinear stage of the evolution of a simple wave

The first two experiments were deliberately performed in a quasilinear setting in the hydrodynamic sector regime, in order to benchmark the numerical scheme. The advantage of the MC-RSW model is that it is capable to treat the fully nonlinear dynamics, including strong shock formation. We therefore choose to study *wave breaking* as a typical nonlinear example. The influence of the nonlinear precipitation on the classical wave breaking and shock formation is of particular interest, as the precipitation term introduces extra dissipation, yet can also produce specific discontinuities.

We consider an initial eastward-propagating simple wave profile identical to the one used in experiment 1 [Eqs. (3.7) and (3.8)] but of higher amplitude: $\epsilon=0.5$ ($\alpha=+1$ and $x_p=4$). The wave propagates through a uniformly dry or uniformly moist (saturated or unsaturated) domain with $Q_s=0.9$.

1. The dry case: $P=0$

We repeat here a standard dry simulation as a benchmark for moist cases treated afterward. The system is given by the usual SW equations and a simple tracer conservation law for humidity Q . The classical wave breaking and shock formation correspond to an intersection between characteristics of the system. This is a weak solution that obeys the RH condition (2.33).

The Hovmöller diagram of the velocity field for the dry simulation (Fig. 13) clearly shows that different parts of the initial profile propagate along characteristics with different speeds $c=u+\sqrt{gh}$. These characteristics intersect each other and produce a shock. The breaking front velocity is not constant and is slightly larger than the unperturbed dry velocity: $s(t) > c_d=1$. A weak westward-propagating simple wave of weak amplitude emerging from the initial perturbation can

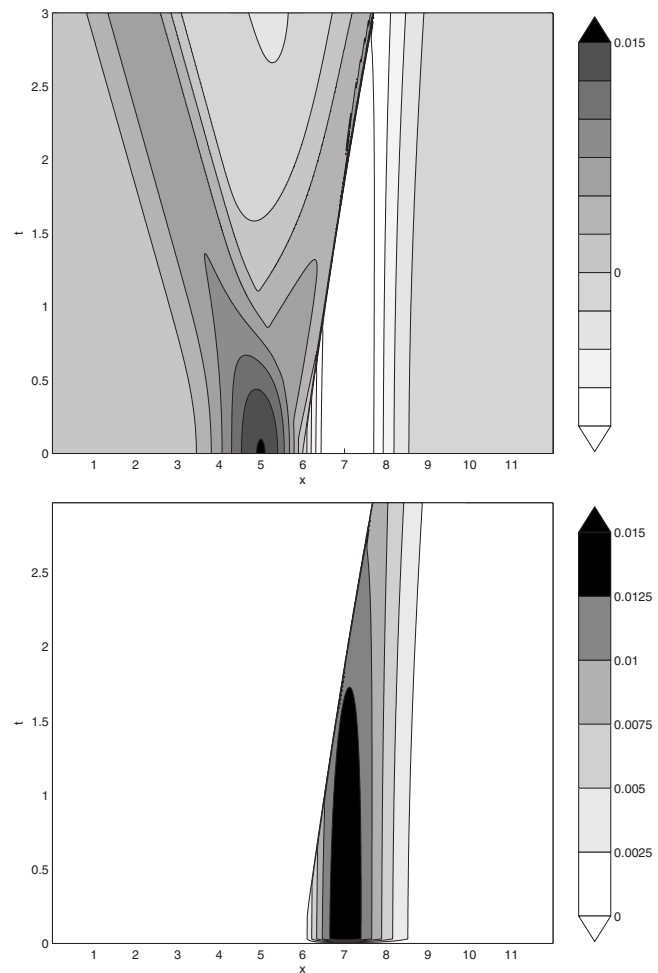


FIG. 11. Same as Fig. 9 but for $Q_s=0.95$. The boundary between precipitating and nonprecipitating regions corresponds to the intersection of dry and moist characteristics. Since $Q_s > 3/4$, the boundary velocity exceeds from the very beginning the moist velocity ($c_m \approx 0.2236$), and a dry subsonic precipitation front arises. $\gamma=5$ and $n_x=1500$.

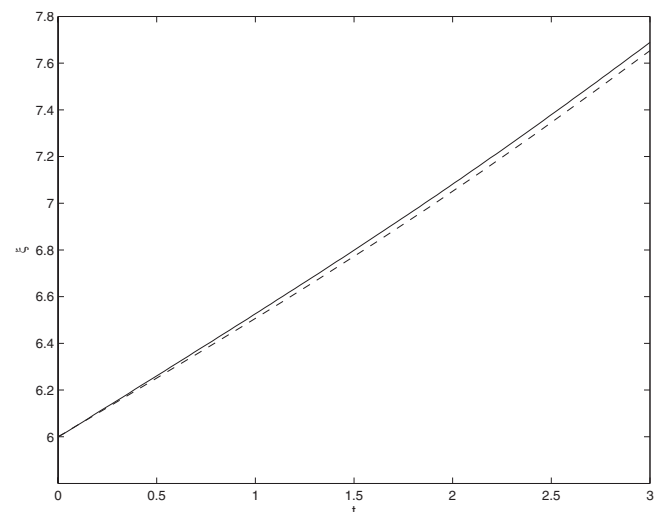


FIG. 12. Same as Fig. 10 but for $Q_s=0.95 > 3/4$. The evolution of the boundary from the DNS (solid) is compared to the solution of the implicit equation for shock condition (dashed) deduced from the analytical results.

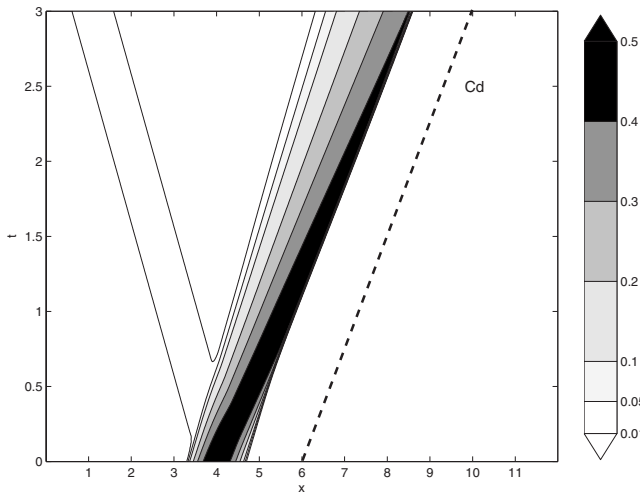


FIG. 13. Hovmöller diagram of the velocity field $u(x,t)$. An eastward-propagating simple wave of significant amplitude is breaking in a dry experiment $P \equiv 0$ ($\epsilon=0.5$, $\alpha=+1$, and $x_p=4$). A shock front emerges with a velocity slightly larger than the unperturbed dry velocity $c_d=1$. $\gamma=5$ and $n_x=1000$.

also be seen. It appears due to nonlinearity because the amplitude of the initial bump is too high to preserve the linearized simple wave condition $\rho_- = 0$, cf. Eq. (3.5).

The time evolution of the spatial profile of the velocity is shown in Fig. 14. The nonlinear steepening and shock formation takes place on the eastern (downstream) side of the initial bump. On the western (upstream) side, emission of a secondary westward-propagating simple wave takes place. Finally, we confirm numerically that wave breaking is a dissipative process as the total energy $E(t)$ starts to decrease once the shock is formed, as shown in Fig. 15.

2. Moist cases

We first consider the uniformly unsaturated case with $Q_0=0.7$, with the same initial simple wave configuration. We can expect that if the wind convergence on its eastern side is

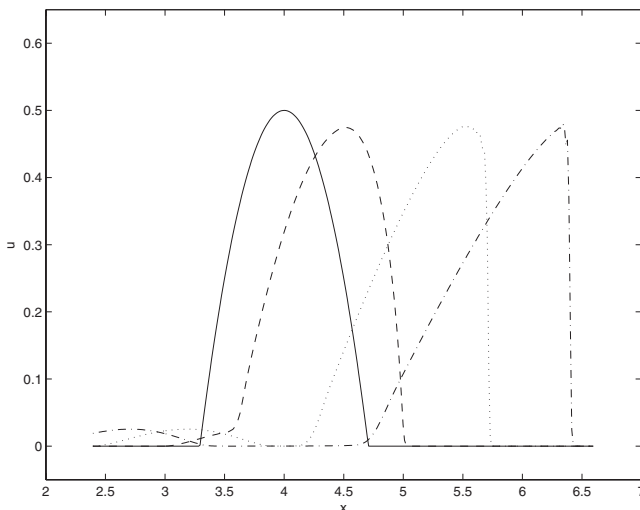


FIG. 14. The profile of the velocity field $u(x,t)$ for different times: $t=0$ (solid), $t=0.3$ (dashed), $t=0.9$ (dotted), and $t=1.4$ (dashed-dotted). Same simulation as in Fig. 13. The shock formation occurs downstream and a secondary westward-propagating simple wave is emitted upstream.

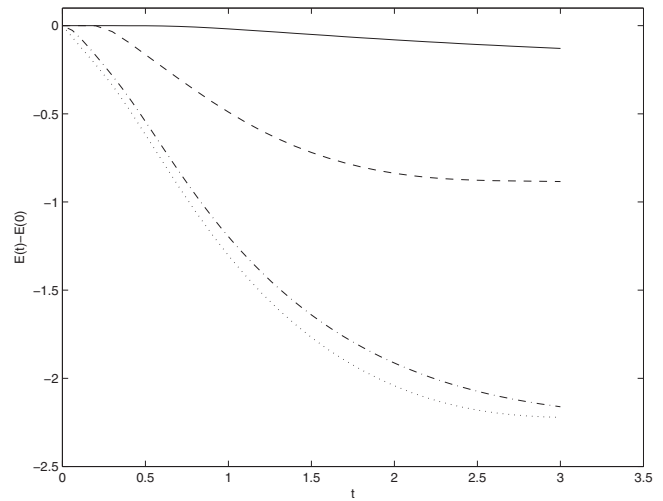


FIG. 15. Time evolution of the deviation of total energy from its initial value $[E(t)-E(0)]$ for the dry wave of Fig. 13 (solid) and the moist cases of Fig. 16 $\{Q_0=0.7, \gamma=5\}$ (dashed), Fig. 19 $\{Q_0=0.9; \gamma=5\}$ (dotted), and Fig. 20 $\{Q_0=0.9, \gamma=100\}$ (dashed-dotted). The dissipated energy in the moist cases is clearly larger than the one only due to wave breaking. This large decrease in energy is associated with precipitation starting at $t \approx 0.25$ for $Q_0=0.7$ and $t=0$ for $Q_0=0.9$.

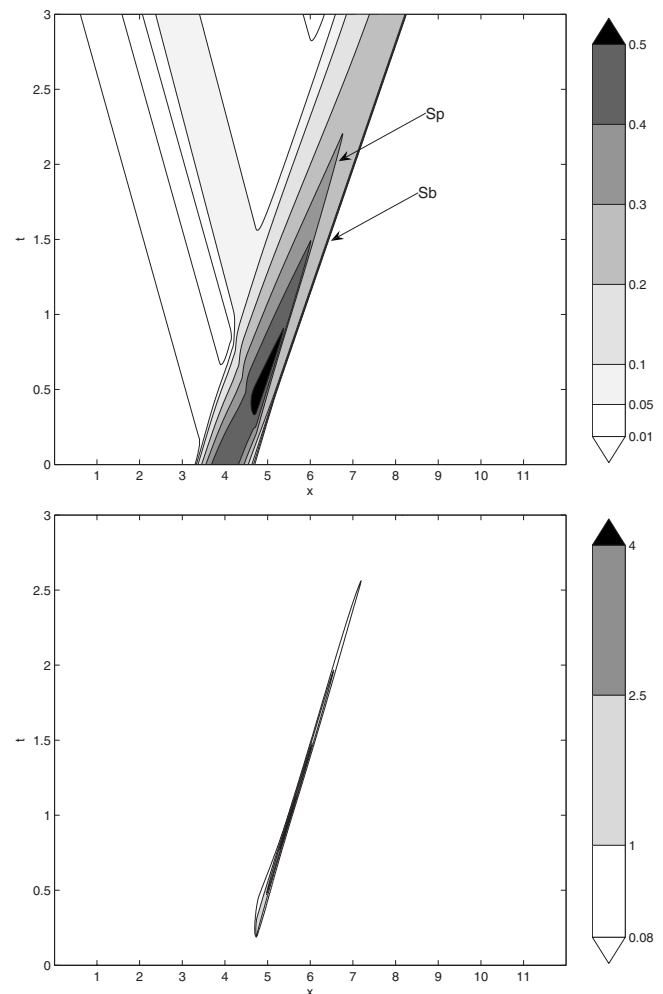


FIG. 16. Hovmöller diagrams of the velocity field $u(x,t)$ (upper panel) and precipitation $P(x,t)$ (lower panel). An eastward-propagating simple wave of significant amplitude is breaking inside a uniformly moist unsaturated domain: $Q_0=0.7$ ($\epsilon=0.5$, $\alpha=+1$, and $x_p=4$). Two fronts emerge: a breaking front ($s_b \approx 1.2$) with a velocity higher than the unperturbed dry velocity $c_d = 1$ and a dry subsonic precipitation front ($s_p \approx 1$) for $t > 0.25$. $\gamma=5$ and $n_x=1000$.

sufficiently strong, the wave triggers precipitation. For rapid relaxation $\gamma=5$, the Hovmöller diagram of the velocity field is shown in Fig. 16. A thin precipitating region, associated with a dry subsonic precipitation front, emerges at $t \approx 0.25$ with a weaker velocity ($s_p \approx 1$) than the breaking front velocity ($s_B \approx 1.2$) (cf. Fig. 17). It is important to remind that the nature of the two fronts is different: The precipitation front is a shock in the gradients only.

As in experiment 1, precipitation partially reflects the initial simple wave since dry Riemann variables are no more constant [cf. Eq. (2.19)]. Consequently, the eastward-propagating characteristic velocities are modified in the precipitating region such that between the two fronts, a plateau in $\{u, h\}$ is formed (see Fig. 18). In this particular nonprecipitating area, the characteristic velocity is thus constant (by constant values of u and h) and is the same as the velocity of the characteristic that is the limit between the group of characteristics affected by precipitation and the group uniquely affected by breaking process. This can be seen in the upper panel of Fig. 17. The moist effects can then change the breaking front velocity, as compared to the dry case. In the present experiment, they make it *slower* (compare Figs. 14 and 18). They also lead to a much more efficient energy dissipation than in the pure breaking process, as shown in Fig. 15.

The question we now ask is whether precipitation can *prevent* wave breaking. We consider the same simple wave propagating inside a uniformly saturated region: $Q_0 = Q_s = 0.9$. One can thus expect that since precipitation starts immediately, the wave is reflected and dissipated before having time to break, as shown in the lower panel of Fig. 17. This is exactly what happens at rapid relaxation ($\gamma=5$) in the Hovmöller diagram of the velocity field for the corresponding simulation (Fig. 19). There still exists a front but uniquely a precipitation one. We compare this experiment with another one with slow relaxation ($\gamma=100$) to confirm the nature of this front (precipitation or breaking front). One sees no front formation in this case (Fig. 20), which means that no breaking occurs for each relaxation and that the lower panel of Fig. 19 represents indeed a precipitation front. This can also be confirmed by the evolution of the spatial profiles of the velocity field presented in Fig. 21.

IV. SUMMARY AND CONCLUDING REMARKS

We studied the dynamical effects of moisture for synoptic-scale motions with the help of a MC-RSW model. The model includes a standard relaxation scheme for precipitation with a relaxation time τ and a convective mass sink. It has the advantages to be fully nonlinear in the hydrodynamic sector, and to be equivalent in its linearized version to previously studied systems.^{6,7,17,18}

The properties of the MC-RSW in 1.5D have been analyzed using the method of characteristics. For finite relaxation time τ , the system is hyperbolic and precipitation modifies the Riemann variables along the characteristic curves: In this case precipitation zones play a role of dissipative reflectors. For immediate relaxation, the system is piecewise hyperbolic. Precipitation is directly linked to wind convergence

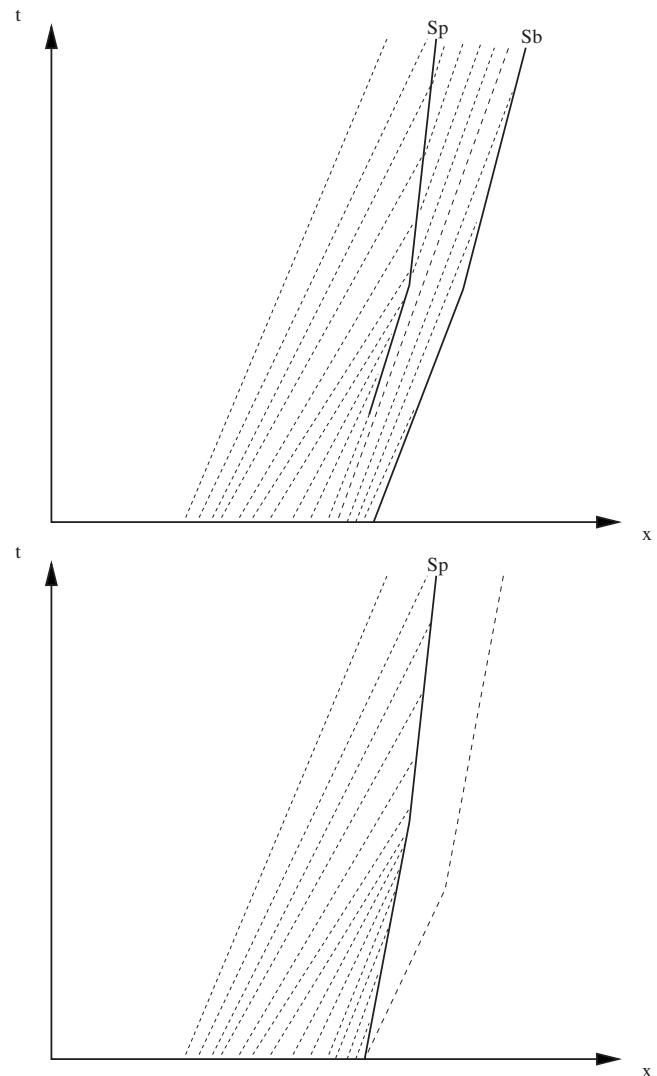


FIG. 17. Sketch of eastward-propagating characteristics for the propagation of a simple wave of significant amplitude in uniformly unsaturated (upper panel) and saturated (lower panel) domains. A precipitation front (s_p) occurs in the approximation of immediate relaxation and prevents the breaking front (s_B) to appear in the saturated case.

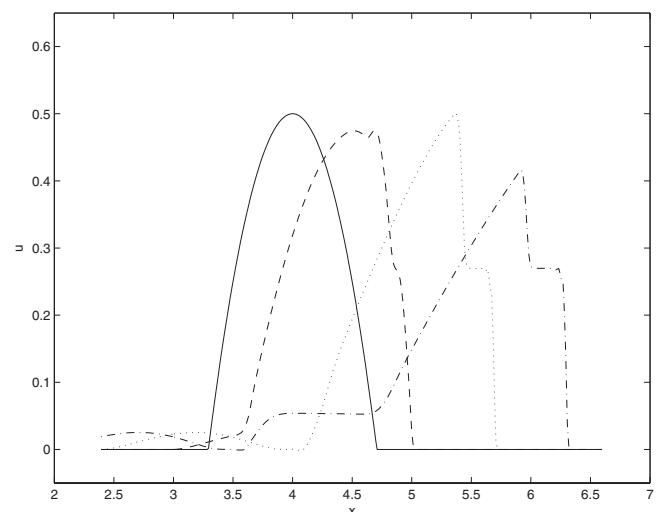


FIG. 18. Spatial profile of the velocity field $u(x, t)$ for different times: $t=0$ (solid), $t=0.3$ (dashed), $t=0.9$ (dotted), and $t=1.4$ (dashed-dotted). Same simulation as in Fig. 16.

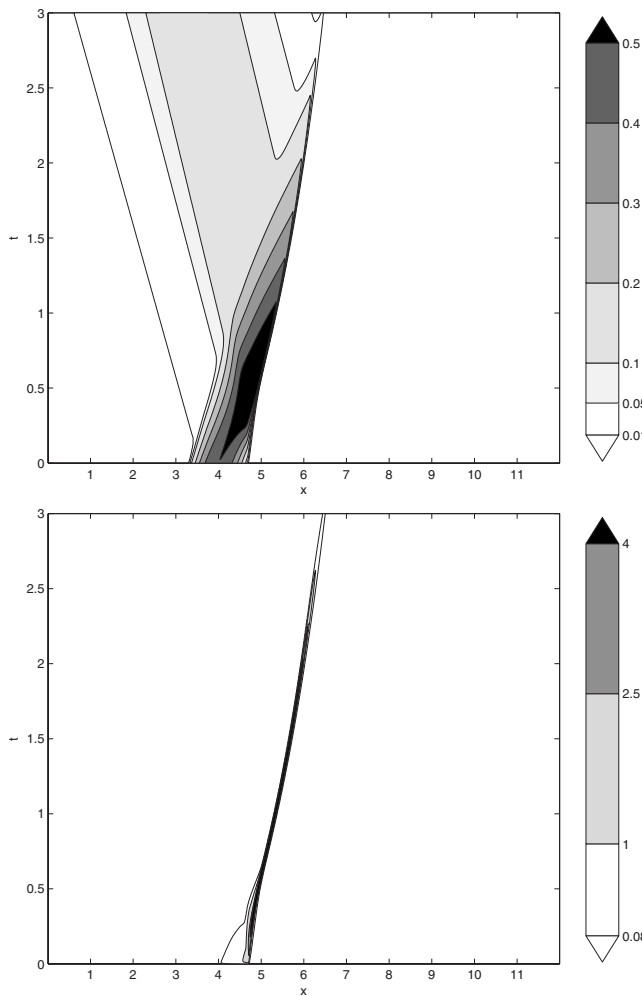


FIG. 19. Hovmöller diagrams of the velocity field $u(x,t)$ (upper panel) and precipitation $P(x,t)$ (lower panel). Same simulation as in Fig. 16 but with $Q_0=Q_s=0.9$. Precipitation starts immediately: A dry subsonic precipitation front emerges and reflects the wave preventing breaking.

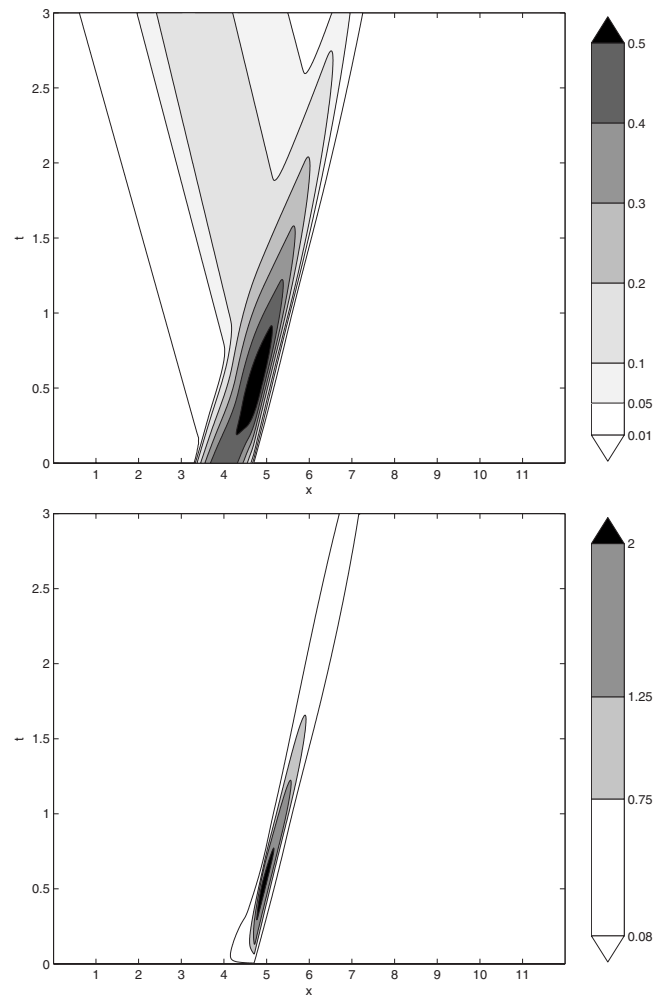


FIG. 20. Hovmöller diagrams of velocity field $u(x,t)$ (upper panel) and precipitation $P(x,t)$ (lower panel). Same simulation as in Fig. 19 but with $\gamma=100$.

such that moist characteristics with slower velocity than in the dry zone emerge in the precipitating region.

In the singular strict quasiequilibrium limit $\tau \rightarrow 0$, the boundary between precipitating and nonprecipitating regions is defined as the intersection between the two different types of characteristics. If a discontinuity in the gradients appears at this boundary, it defines a precipitation front. The corresponding RH conditions have been derived for the MC-RSW in 1.5D leading to a nonlinear generalization of the three types of precipitation fronts found in Ref. 6.

A numerical implementation of the MC-RSW model was proposed using a finite-volume scheme²⁰ developed for SW equations, supplied with a Betts–Miller-type parametrization of the precipitation and related latent heat release. A series of numerical experiments was performed with this model, allowing to (1) benchmark the numerical scheme by comparing it with known theoretical results with quasilinear dynamics in the hydrodynamical sector and (2) reveal new dynamical effects when hydrodynamic and phase-transition nonlinearities are combined. Thus, we identified rapid and slow relaxation regimes by studying the scattering of a

simple wave on the moisture front. The results of our experiments confirm the dissipative reflector role played by the moist regions. We also investigated and classified conditions of emergence of precipitation fronts, thus completing and extending the results of Gill.¹⁷ Finally, we studied the role of humidity in wave steepening and shock formation that is essentially a nonlinear hydrodynamic phenomenon, and showed how precipitation attenuates, and even arrests wave breaking.

Thus, the MC-RSW model appears as a simple and adequate tool for analyzing the effects of precipitation in fully nonlinear dynamics. It allows for further improvements, such as including β -effect and topography, while maintaining the efficiency of numerical simulations.

It should be stressed, however, that MC-RSW is not a realistic model of the lower troposphere because of the severe constraint of the adiabaticity imposed as a part of the closure, as discussed in Appendix A. It should be rather considered as an effective lower-layer dynamics of the full two- or multilayer baroclinic model, which can be derived along the same lines and will be presented elsewhere.

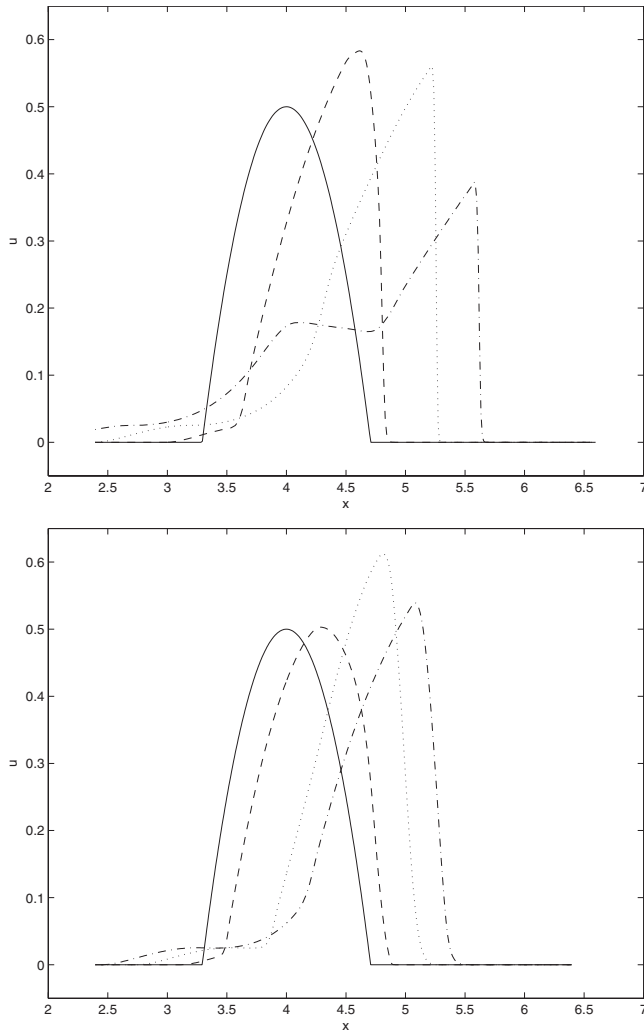


FIG. 21. Spatial profile of velocity field $u(x,t)$ for different times: $t=0$ (solid), $t=0.3$ (dashed), $t=0.9$ (dotted), and $t=1.4$ (dashed-dotted). Same simulation as in Fig. 19 (upper panel) and Fig. 20 (lower panel).

ACKNOWLEDGMENTS

We are grateful to S. Medvedev for collaboration on the theoretical aspects of the MC-RSW on early stages of this work. The first numerical tests with the MC-RSW model were performed by A. Casado-Lopez during his master thesis (University Paris VI, 2007), which is also gratefully acknowledged. V.Z. thanks A. Majda for stimulating discussions. G.L. was supported by an ANR grant (ENVISTORM, Grant No. JCJC06-139163). We are also grateful to the anonymous referees for constructive remarks on the first version of the paper.

APPENDIX A: MOIST ENTHALPY CONSERVATION PRINCIPLE AND “MOIST RIPA’S” MODEL

As it was already mentioned in the main text, the ME conservation may be used as a guiding principle in deriving simplified moist-convective models. Lagrangian conservation of ME on the isobaric surface is written as $(d\theta/dt) + (L/c_p)(dq/dt) = 0$, where d/dt is Lagrangian derivative, θ is

the potential temperature, q is the specific humidity, and L and c_p are the latent and specific heats, respectively. Integrated over the fluid layer this gives

$$\int_{z_1}^{z_2} dz \left[\frac{d\theta}{dt} + \frac{L}{c_p} \frac{dq}{dt} \right] = 0. \quad (\text{A1})$$

Introducing the vertical averages denoted by angles, and supposing, as in the main text, that convective velocity W is allowed through the upper boundary, we find for the first term in Eq. (A1),

$$\begin{aligned} \int_{z_1}^{z_2} dz \frac{d\theta}{dt} &= \partial_t(\langle \theta \rangle h) + \nabla \cdot (\langle \mathbf{v} \rangle \langle \theta \rangle h) - \left(\frac{dz_2}{dt} - w(z_2) \right) \theta(z_2) \\ &\quad + \left(\frac{dz_1}{dt} - w(z_1) \right) \theta(z_1), \\ &= \Delta[\langle \theta \rangle h] + W\theta(z_2), \end{aligned} \quad (\text{A2})$$

where we define $\Delta[A] = \partial_t A + \nabla \cdot (\langle \mathbf{v} \rangle A)$. The second term is treated analogously and we arrive to the following conservation law:

$$\Delta[\langle \theta \rangle h] + \frac{L}{c_p} \Delta[Q] + W \left(\theta(z_2) + \frac{L}{c_p} q(z_2) \right) = 0. \quad (\text{A3})$$

The relation between h and W is obtained from the vertically averaged continuity equation,

$$W = -[\partial_t h + \nabla \cdot (\langle \mathbf{v} \rangle h)] = -\Delta[h]. \quad (\text{A4})$$

We therefore find that

$$\Delta[\langle \theta \rangle h] + \frac{L}{c_p} \Delta[Q] - \Delta[h] \left(\theta(z_2) + \frac{L}{c_p} q(z_2) \right) = 0. \quad (\text{A5})$$

The standard assumption in the derivation of the RSW models (2.2) and (2.3) from the primitive equations in pseudoheight coordinates was the constancy of the mean potential temperature over the layer: $\langle \theta \rangle = \theta \approx \theta_0$. Under this assumption Eq. (A3) is equivalent to the local conservation of humidity,

$$\frac{L}{c_p} \Delta[Q - q(z_2)h] = 0, \quad (\text{A6})$$

with $q(z_2) = \text{const}$. By combining Eqs. (A4) and (A6) we get an explicit relation between W and P : $W = [1/q(z_2)]P$.

We see that the standard SW hypothesis is severely restricting the thermodynamics of the model, and it is natural to try to relax it. It is known that the SW equations obtained by vertical averaging of the dry primitive equations by considering the averaged potential temperature of the layer to be variable contain an additional term in the right hand side of the momentum equation,

$$-\frac{g}{\theta_0} \frac{h \nabla \langle \theta \rangle}{2}. \quad (\text{A7})$$

This term allows to include the thermodynamic effects into dynamics, and in the absence of moisture and precipitation Ripa’s model^{25,26} follows. It was initially introduced in the oceanographic context precisely to include thermodynamic

effects. If moisture is added to the model, it seems natural to introduce a source term corresponding to the latent heat release in the potential temperature equation and to conserve mass. Thus

$$\langle \theta \rangle \neq \text{const} \quad \text{and} \quad W = 0, \quad (\text{A8})$$

and the ME conservation gives

$$\Delta \left[\langle \theta \rangle h + \frac{L}{c_p} Q \right] = 0. \quad (\text{A9})$$

The choice of sources and sinks for Q and $\langle \theta \rangle$ is obvious,

$$\Delta[Q] = -P \Rightarrow \Delta[\langle \theta \rangle h] = + \frac{L}{c_p} P \Rightarrow \frac{d}{dt} \langle \theta \rangle = + \frac{L}{c_p h} P, \quad (\text{A10})$$

and omitting angles we arrive to the moist Ripa's model,

$$\partial_t \mathbf{v} + (\mathbf{v} \cdot \nabla) \mathbf{v} = - \frac{g}{\theta_0} \left(\theta \nabla h + \frac{h \nabla \theta}{2} \right) - f \mathbf{k} \times \mathbf{v}, \quad (\text{A11})$$

$$\partial_t h + \nabla \cdot (\mathbf{v} h) = 0, \quad (\text{A12})$$

$$\partial_t \theta + (\mathbf{v} \cdot \nabla) \theta = \frac{L}{c_p h} P, \quad (\text{A13})$$

$$\partial_t Q + \nabla \cdot (\mathbf{v} Q) = -P. \quad (\text{A14})$$

As compared to the MC-RSW model of Sec. II A, which may be called *adiabatic convective*, this model physically means that latent heat release due to precipitation increases the average potential temperature of the fluid layer instead of ejecting convective plumes through the upper boundary (a *diabatic nonconvective* model).

As in the MC-RSW model, we can consider now the immediate relaxation limit for the precipitation term and obtain the associated characteristic equations in the precipitating regions ($P = -Q_s \nabla \cdot \mathbf{v} > 0$). This allows to find the moist characteristic velocity c_m . Considering the 1D version of Eqs. (A11)–(A14) one can easily show that this latter is *faster than* c_d ,

$$c_m = \sqrt{\frac{g}{\theta_0} \left(\theta h + \frac{LQ}{2c_p} \right)} > c_d = \sqrt{\frac{g}{\theta_0} \theta h}. \quad (\text{A15})$$

This contradicts the observations that display moisture-coupled waves which are slower than ordinary gravity waves. The result does not change if one introduces a background stratification in temperature and humidity: $a_{\text{tot}}(x, y, z, t) = a_0 + a_s(z) + a(x, y, z, t)$ for $a = \{\theta, q\}$ before vertical averaging.

Thus, at least in the simplest one-layer setting without mass fluxes through the vertical boundaries, Ripa's atmospheric model, although self-consistent per se, is not compatible with the standard physics, nor with the linearized models studied in literature, and should be discarded. The explanation of this fact is the effective barotropic character of the moist Ripa's model. At the same time, the MC-RSW model used in the main text mimics baroclinicity by allowing the

extra mass flux through the upper boundary, and thus should be rather interpreted as a lower-layer dynamics of the full multilayer model.

Let us mention finally that convective mass flux may be added to the moist Ripa's model (a *diabatic convective* model). However, additional *ad hoc* hypotheses are needed in this case to fix unambiguously the convective mass sink and the latent heat source originating from the precipitation sink in the moisture equation, although certain choices, e.g., $\Delta[\langle \theta \rangle h] = 0$, may give correct relation between dry and moist characteristic velocities.

APPENDIX B: NONCONSTANT SATURATION VALUE Q_s IN THE BETTS–MILLER SCHEME

As the reference convective profile depends on the vertical coordinates, $q^c(z)$, in the original Betts–Miller scheme,³ we may expect that its vertical average depends on the layer thickness in Eq. (2.8). As a first approximation, we can assume

$$Q_s = \int_{z_1}^{z_2} q^c(z) dz \approx \bar{Q} - \alpha \eta, \quad (\text{B1})$$

where \bar{Q} is a constant and $\alpha \eta$ is the deviation from it in term of the free surface displacement η from the basic state H_0 . This linear term is also referred as CAPE (convectively available potential energy)-parametrization if we use the analogy between η and the (potential) temperature disturbance.⁶

In this case, it is easy to show that all the results obtained in the main text still hold. Modifications appear just in the expressions of the precipitation term and the moist speed for immediate relaxation with respect to the choice of constant Q_s ,

$$P_{\tau \rightarrow 0} = - \frac{\bar{Q} + \alpha H_0}{1 + \alpha \beta} \nabla \cdot \mathbf{v} \quad (\text{B2})$$

and

$$c_m = \sqrt{g \left(\frac{H_0 - \beta \bar{Q}}{1 + \alpha \beta} + \eta \right)} \quad (\text{B3})$$

consistent with Ref. 4.

APPENDIX C: NUMERICAL PARAMETRIZATION OF PRECIPITATION

The treatment of moisture follows the same procedure as for the other variables since in the absence of precipitation, it is the equation of a conserved scalar. After the dynamical tendencies of water vapor Q and the thickness h have been added to compute the new (intermediate) values \tilde{Q}_i^{n+1} and \tilde{h}_i^{n+1} , the precipitation is evaluated via the relation

$$P_i^{n+1} = \begin{cases} \frac{\tilde{Q}_i^{n+1} - Q_s}{\tau} & \text{if } \tilde{Q}_i^{n+1} > Q_s \\ 0 & \text{if } \tilde{Q}_i^{n+1} \leq Q_s, \end{cases} \quad (\text{C1})$$

with $\tau = \gamma \Delta t$. Then water vapor and layer thickness are updated following

$$Q_i^{n+1} = \tilde{Q}_i^{n+1} - P_i^{n+1} \Delta t, \quad (\text{C2})$$

$$h_i^{n+1} = \tilde{h}_i^{n+1} - \beta P_i^{n+1} \Delta t. \quad (\text{C3})$$

- ¹I. M. Held and B. J. Soden, "Water vapor feedback and global warming," *Annu. Rev. Energy Environ.* **25**, 441 (2000).
- ²A. Arakawa and W. H. Schubert, "Interaction of a cumulus cloud ensemble with the large-scale environment, Part 1," *J. Atmos. Sci.* **31**, 674 (1974).
- ³A. K. Betts and M. J. Miller, "A new convective adjustment scheme. Part II: Single columns tests using GATE wave, BOMEX, ATEX and arctic air-mass data sets," *Q. J. R. Meteorol. Soc.* **112**, 693 (1986).
- ⁴G. Lapeyre and I. M. Held, "The role of moisture in the dynamics and energetics of turbulent baroclinic eddies," *J. Atmos. Sci.* **61**, 1693 (2004).
- ⁵O. Rivière, G. Lapeyre, and O. Talagrand, "A novel technique for nonlinear sensitivity analysis: Application to moist predictability," *Q. J. R. Meteorol. Soc.* **135**, 1520 (2009).
- ⁶D. M. W. Frierson, A. J. Majda, and O. M. Pauluis, "Large scale dynamics of precipitation fronts in the tropical atmosphere: A novel relaxation limit," *Commun. Math. Sci.* **2**, 591 (2004).
- ⁷O. Pauluis, D. M. W. Frierson, and A. J. Majda, "Precipitation fronts and the reflection and transmission of tropical disturbances," *Q. J. R. Meteorol. Soc.* **134**, 913 (2008).
- ⁸A. K. Emanuel, J. D. Neelin, and C. S. Bretherton, "On large-scale circulations in convecting atmosphere," *Q. J. R. Meteorol. Soc.* **120**, 1111 (1994).
- ⁹A. K. Emanuel, *Atmospheric Convection* (Oxford University Press, Oxford, 1994), Chap. 4.
- ¹⁰J. D. Neelin and N. Zeng, "A quasi-equilibrium tropical circulation model—Formulation," *J. Atmos. Sci.* **57**, 1741 (2000).
- ¹¹N.-C. Lau, I. M. Held, and J. D. Neelin, "The Madden-Julian oscillation in an idealized general circulation model," *J. Atmos. Sci.* **45**, 3810 (1988).
- ¹²J. G. Charney and A. Eliassen, "On the growth of the hurricane depression," *J. Atmos. Sci.* **21**, 68 (1964).
- ¹³A. K. Emanuel, M. Fantini, and A. J. Thorpe, "Baroclinic instability in an environment of small stability to slantwise moist convection. Part I: Two-dimensional models," *J. Atmos. Sci.* **44**, 1559 (1987).
- ¹⁴D. J. Parker and A. J. Thorpe, "Conditional convective heating in a baroclinic atmosphere: A model of convective frontogenesis," *J. Atmos. Sci.* **52**, 1699 (1995).
- ¹⁵H. L. Kuo, "On formation and intensification of tropical cyclones through latent heat release by cumulus convection," *J. Atmos. Sci.* **22**, 40 (1965).
- ¹⁶Y. Hayashi and D. G. Golder, "United mechanisms for the generation of low- and high-frequency tropical waves. Part I: Control experiments with moist convective adjustment," *J. Atmos. Sci.* **54**, 1262 (1997).
- ¹⁷A. E. Gill, "Studies of moisture effects in simple atmospheric models: The stable case," *Geophys. Astrophys. Fluid Dyn.* **19**, 119 (1982).
- ¹⁸S. N. Stechmann and A. J. Majda, "The structure of precipitation fronts for finite relaxation time," *Theor. Comput. Fluid Dyn.* **20**, 377 (2006).
- ¹⁹J. Dias and O. Pauluis, "Convectively coupled waves propagating along an equatorial ITCZ," *J. Atmos. Sci.* **66**, 2237 (2009).
- ²⁰F. Bouchut, "Efficient numerical finite volume schemes for shallow water models," in *Nonlinear Dynamics of Rotating Shallow Water: Methods and Advances*, edited by V. Zeitlin (Elsevier, Amsterdam, 2007), Chap. 4.
- ²¹V. Zeitlin, "Nonlinear wave phenomena in rotating shallow water with applications to geostrophic adjustment," in *Nonlinear Dynamics of Rotating Shallow Water: Methods and Advances*, edited by V. Zeitlin (Elsevier, Amsterdam, 2007), Chap. 5.
- ²²J. Yano, J. C. McWilliams, M. W. Moncrieff, and K. A. Emanuel, "Hierarchical tropical cloud systems in an analog shallow-water model," *J. Atmos. Sci.* **52**, 1723 (1995).
- ²³D. A. Schecter and T. J. Dunkerton, "Hurricane formation in diabatic Ekman turbulence," *Q. J. R. Meteorol. Soc.* **135**, 823 (2009).
- ²⁴V. Zeitlin, "Introduction: Fundamentals of rotating shallow water model in the geophysical fluid dynamics perspective," in *Nonlinear Dynamics of Rotating Shallow Water: Methods and Advances*, edited by V. Zeitlin (Elsevier, Amsterdam, Oxford, 2007), Chap. 1.
- ²⁵P. Ripa, "Conservation laws for primitive equations models with inhomogeneous layers," *Geophys. Astrophys. Fluid Dyn.* **70**, 85 (1993).
- ²⁶P. Ripa, "On improving a one-layer ocean model with thermodynamics," *J. Fluid Mech.* **303**, 169 (1995).
- ²⁷B. J. Hoskins and F. P. Bretherton, "Atmospheric frontogenesis models: Mathematical formulation and solution," *J. Atmos. Sci.* **29**, 11 (1972).
- ²⁸O. Marchal and J. Nycander, "Nonuniform upwelling in a shallow-water model of the Antarctic bottom water in the Brazil Basin," *J. Phys. Oceanogr.* **34**, 2492 (2004).
- ²⁹A. E. Gill, "Some simple solutions for heat-induced tropical circulation," *Q. J. R. Meteorol. Soc.* **106**, 447 (1980).
- ³⁰W. A. Heckley and A. E. Gill, "Some simple analytical solutions to the problem of forced equatorial long waves," *Q. J. R. Meteorol. Soc.* **110**, 203 (1984).
- ³¹C. S. Bretherton and A. H. Sobel, "The Gill model and the weak temperature gradient approximation," *J. Atmos. Sci.* **60**, 451 (2003).
- ³²A. H. Sobel, J. Nilsson, and L. M. Polvani, "The weak temperature gradient approximation and balanced tropical moisture waves," *J. Atmos. Sci.* **58**, 3650 (2001).
- ³³G. B. Whitham, *Linear and Nonlinear Waves* (Wiley, New York, 1974), Chap. 5.
- ³⁴F. X. Crum and T. J. Dunkerton, "Analytic and numerical models of wave-CISK with conditional heating," *J. Atmos. Sci.* **49**, 1693 (1992).
- ³⁵V. Zeitlin, S. Medvedev, and R. Plougonven, "Frontal geostrophic adjustment, slow manifold, and nonlinear wave phenomena in one-dimensional rotating shallow water. Part 1. Theory," *J. Fluid Mech.* **481**, 269 (2003).
- ³⁶F. Bouchut, J. LeSommer, and V. Zeitlin, "Frontal geostrophic adjustment, slow manifold, and nonlinear wave phenomena in one-dimensional rotating shallow water. Part 2. High-resolution numerical simulations," *J. Fluid Mech.* **514**, 35 (2004).
- ³⁷F. Bouchut, E. Scherer, and V. Zeitlin, "Nonlinear adjustment of a front over escarpment," *Phys. Fluids* **20**, 016602 (2008).
- ³⁸M. Wheeler and G. N. Kiladis, "Convectively coupled equatorial waves: analysis of clouds and temperature in the wavenumber-frequency domain," *J. Atmos. Sci.* **56**, 374 (1999).